Evolutionary dynamics of bacteria in the gut microbiome within and across hosts

Nandita R. Garud[1]◑*, Benjamin H. Good[2,3,5,]◑*, Oskar Hallatschek[2,4,5], Katherine S. Pollard[1,6,7]

1 Gladstone Institutes, San Francisco, California, United States of America
2 Department of Physics, University of California, Berkeley, California, United States of America
3 Department of Bioengineering, University of California, Berkeley, California, United States of America
4 Department of Integrative Biology, University of California, Berkeley, California, United States of America
5 Kavli Institute for Theoretical Physics, University of California, Santa Barbara, California, United States of America
6 Department of Epidemiology & Biostatistics, Institute for Human Genetics, Quantitative Biology Institute, and Institute for Computational Health Sciences, University of California, San Francisco, California, United States of America
7 Chan-Zuckerberg Biohub, San Francisco, California, United States of America

◑These authors contributed equally and are ordered alphabetically
* benjamin.h.good@berkeley.edu (B.H.G.), nandita.garud@gladstone.ucsf.edu (N.R.G.)

Abstract

Gut microbiota are shaped by a combination of ecological and evolutionary forces. While the ecological dynamics have been extensively studied, much less is known about how species of gut bacteria evolve over time. Here we introduce a model-based framework for quantifying evolutionary dynamics within and across hosts using a panel of metagenomic samples. We use this approach to study evolution in ∼30 prevalent species in the human gut. Although the patterns of between-host diversity are consistent with quasi-sexual evolution and purifying selection on long timescales, we identify new genealogical signatures that challenge standard population genetic models of these processes. On shorter timescales within hosts, we find that genetic differences only rarely arise from the invasion of distantly related strains. Instead, the resident strains more commonly acquire a smaller number of evolutionary changes, in which nucleotide variants or gene gains or losses rapidly sweep to high frequency over ∼6 month timescales. By comparing these mutations with the typical between-host differences, we find evidence that sweeps are driven by introgression from other strains, rather than by new mutations. Our results suggest that gut bacteria evolve on human-relevant timescales, and highlight the feedback between short- and long-term evolution across hosts.

Introduction

The gut microbiome is a complex ecosystem comprised of a diverse array of microbial organisms. The abundances of different species and strains can vary dramatically based on diet [1], host-species [2], and the identities of other co-colonizing taxa [3]. These rapid shifts in community composition suggest that individual gut microbes may be adapted to specific environmental conditions, with strong selection pressures between competing species or strains. Yet while these ecological responses have been extensively studied, much less is known about the evolutionary forces that operate within populations of gut bacteria, both within individual hosts, and across the larger host-associated population. This makes it difficult to predict how rapidly strains of gut microbes will evolve new ecological preferences when faced with environmental challenges, like drugs or diet, and how the genetic composition of the community will change as a result.

The answers to these questions depend on two different types of information. At a mechanistic level, one must understand the functional traits that are under selection in the gut, and how they may be modified genetically. Recent work has started to address this question, leveraging techniques from comparative genomics [4–6], evolution in model organisms [7–9], and high-throughput genetic screens [10, 11]. Yet in addition to the targets of selection, evolution also depends on population genetic processes that describe how mutations spread through a population of gut bacteria, both within individual hosts, and across the larger population. These dynamical processes can strongly influence which mutations are likely fix within a population, and the levels of genetic diversity that such populations can maintain. Understanding these processes is the goal of our present work.

Previous studies of pathogens [12], laboratory evolution experiments [13], and some environmental communities [14–17] have shown that microbial evolutionary dynamics are often dominated by rapid adaptation, with new variants accumulating within months or years [7, 14, 18–25]. However, it is not clear how this existing picture of microbial evolution extends to a more complex and established ecosystem like the healthy gut microbiome. On the one hand, hominid gut bacteria have had many generations to adapt to their host environment [26], and may not be subject to the continually changing immune pressures faced by many pathogens. The large number of potential competitors in the gut ecosystem may also provide fewer opportunities for a strain to adapt to new conditions before an existing strain expands to fill the niche [27, 28] or a new strain invades from outside the host. On the other hand, it is also possible that small-scale environmental fluctuations, either driven directly by the host or through interactions with other resident strains, might increase the opportunities for local adaptation [29]. If immigration is restricted, the large census population size of gut bacteria could allow residents to produce and fix adaptive variants rapidly before a new strain is able to invade. In this case, one might expect to observe rapid adaptation on short timescales, which is eventually arrested on longer timescales as strains are exposed to the full range of host environments. Determining which of these scenarios apply to gut communities is critical for efforts to study and manipulate the microbiome.

While traditional amplicon sequencing provides limited resolution to detect within-species evolution [30], whole-genome shotgun metagenomic sequencing is starting to provide the raw polymorphism data necessary to address these questions [31]. In particular, several reference-based approaches have been developed to detect genetic variants within individual species in larger metagenomic samples [31–36]. While these approaches enable strain-level comparisons between samples, they have also documented substantial within-species variation in individual metagenomes [31, 35, 37], suggesting that the bacteria derive from sub-populations rather than single clones. This makes it difficult to assign an evolutionary interpretation to the genetic differences between samples, since they arise from unobserved mixtures of different bacterial lineages.

Several approaches have been developed to further resolve these mixed populations into individual haplotypes or "strains". These range from simple consensus approximations [35,37,38], to sophisticated clustering algorithms [39,40] and the incorporation of physical linkage information [41]. However, while these ad-hoc methods are useful for tracking well-defined strains across

samples, it is not known how their assumptions and failure modes might bias inferences of evolutionary dynamics, particularly among closely related strains. As a result, the evolutionary processes that operate within species of gut bacteria remain poorly characterized.

In this study, we take a different approach to the strain detection problem, which is specifically designed for inferring evolutionary dynamics in a large panel of metagenomes. Building on earlier work by [4, 35], we show that many prevalent species have a subset of hosts for which a portion of the dominant lineage is much easier to identify. By focusing only on this subset of "quasi-phaseable" samples, we develop methods for resolving small differences between the dominant lineages with a high degree of confidence.

We use this approach to analyze a large panel of publicly available human stool samples [42–44], which allows us to quantify evolutionary dynamics within and across hosts in ∼30 prevalent bacterial species. We find that the long-term evolutionary dynamics across hosts are broadly consistent with models of quasi-sexual evolution and purifying selection, with relatively weak geographic structure in many prevalent species. However, our quantitative approach also reveals interesting departures from standard population genetic models of these processes, which suggests that new models are required to fully understand the evolutionary dynamics that take place across the larger population.

We also use our approach to detect examples of within-host adaptation, in which nucleotide variants or gene gains or losses rapidly sweep to high frequency within ∼6 month intervals. We find evidence that many of these within-host sweeps are driven by introgression from existing species or strains, rather than by *de novo* mutations, consistent with the hypothesis that there are many such routes for adaptation in a complex ecosystem with large census population sizes and frequent horizontal exchange. Together, these results show that the gut microbiome is a promising system for studying the dynamics of microbial evolution in a complex community setting. The framework we introduce may also be useful for characterizing evolution of microbial communities in other environments.

Results

Resolving within-host lineage structure in a panel of metagenomic samples

To investigate evolutionary dynamics within species in the gut microbiome, we analyzed shotgun metagenomic data from a panel of stool samples from 365 healthy individuals sequenced in previous work (Table S1). This panel includes 180 North American subjects sequenced by the Human Microbiome Project [42, 44], a subset of which were sampled at 2 or 3 timepoints roughly 6-12 months apart. To control for geographic structure, we also included samples from 185 Chinese subjects sequenced at a single timepoint. We used a standard reference-based approach to measure single nucleotide variant (SNV) frequencies and gene copy number across a panel of prevalent species for each metagenomic sample (Methods). Descriptive summaries of this genetic variation have been reported elsewhere [31, 33–35, 37, 44]. Here, we revisit these patterns to investigate how they emerge from the lineage structure set by the host colonization process. Using these results, we then show how certain aspects of this lineage structure can be inferred from the statistics of within-host polymorphism, which enable measurements of evolutionary dynamics across samples.

As an illustrative example, we first focus on the patterns of polymorphism in *Bacteroides vulgatus*, which is among the most abundant and prevalent species in the human gut. These properties ensure that the *B. vulgatus* genome has high-coverage in many samples, which enables more precise estimates of the allele frequencies in each sample (Fig. 1A-D). The overall levels of within-host diversity for this species are summarized in Fig. 1E, based on the fraction of synonymous sites in core genes with intermediate allele frequencies (white region in Figs. 1A-D). The rate of intermediate-frequency polymorphism varies widely among the samples: some metagenomes have only a few variants along the *B. vulgatus* genome, while others have mutations

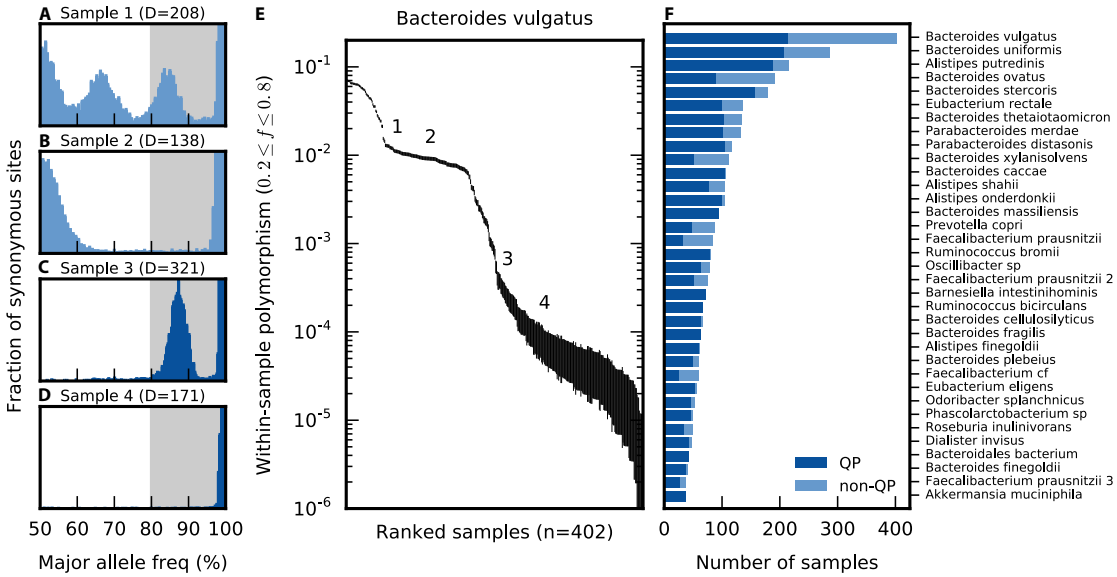

Fig 1. Genetic diversity within hosts. (a-d) The distribution of major allele frequencies at synonymous sites in the core genome of *Bacteroides vulgatus* for four different samples, with the median core-genome-wide read depth D listed above each panel. To emphasize the distributional patterns, the vertical axis is scaled by an arbitrary normalization constant in each panel, and it is truncated for visibility. (e) The average fraction of synonymous sites in the core genome with major allele frequencies $\leq 80\%$, for different samples of *B. vulgatus*. Vertical lines denote 95% posterior confidence intervals based on the observed number of counts (SI Section S9 Text). For comparison, the corresponding values for the samples in panels (a-d) are indicated by the numbers (1-4). (f) The distribution of quasi-phaseable (QP) samples among the 35 most prevalent species, arranged by descending prevalence; the distribution across hosts is shown in Fig. S4. For comparison, panels (c) and (d) are classified as quasi-phaseable, while panels (a) and (b) are not.

at more than 1% of all synonymous sites (comparable to the differences between samples, Fig. S2).

We first asked whether these patterns are consistent a model in which each host is colonized by a single *B. vulgatus* clone, so that the intermediate frequency variants represent mutations that have arisen since colonization. Assuming this model and using conservatively high estimates for per site mutation rates ($\mu \sim 10^{-9}$ [45]), generation times (~ 10 per day [46]), and time since colonization (< 100 years), we estimate a neutral polymorphism rate $< 10^{-3}$ at each synonymous site (SI Section S2 Text), which is at odds with the higher levels of diversity in many samples (Fig. 1E). Instead, we conclude that the samples with higher synonymous diversity must have been colonized by multiple divergent bacterial lineages that accumulated mutations for many generations before coming together in the same gut community.

As a plausible alternative, we next asked whether the data are consistent with a large number of colonizing lineages ($n_c \gg 1$) drawn at random from the broader population. However, this process is expected to produce fairly consistent polymorphism rates and allele frequency distributions in different samples, which is at odds with the variability we observe even among the high-diversity samples (e.g., Figs. 1A,B). Instead, we hypothesize that many of the high-diversity hosts have been colonized by just a few diverged lineages [i.e., $(n_c - 1) \sim O(1)$]. Consistent with this hypothesis, the distribution of allele frequencies in each host is often strongly peaked around a few characteristic frequencies (Fig. 1A-D), suggesting a mixture of several distinct lineages. Similar findings have recently been reported in a number of other host-associated microbes, including several species of gut bacteria [4, 35, 47, 48]. Figures 1A-C show that hosts can vary both in the apparent number of colonizing lineages, and the frequencies at which they are mixed together. As a result, we cannot exclude the possibility that even the low diversity samples (e.g.

Fig. 1D) are colonized by multiple lineages that happen to fall below the detection threshold set by the depth of sequencing. We will refer to samples with a small number of diverged lineages as an "oligo-colonization" model, in order to contrast with the single-colonization ($n_c = 1$) and multiple-colonization ($n_c \gg 1$) alternatives above.

Quasi-phaseable (QP) samples

Compared to the single- and multiple-colonization models, the oligo-colonization model makes it more difficult to identify evolutionary changes between lineages. In this scenario, individual hosts are not clonal, but the within-host allele frequencies derive from idiosyncratic colonization processes, rather than a large random sample from the population. To disentangle genetic changes between lineages from these host-specific factors, we must estimate phased haplotypes (or "strains") from the distribution of allele frequencies within individual hosts. This is a complicated inverse problem, and we will not attempt to solve the general case here. Instead, we adopt an approach similar to Ref. [35] and others, and leverage the fact that the lineage structure in *certain* hosts is sufficiently simple that we can assign alleles to the dominant lineage with a high degree of confidence.

Our approach is based on the simple observation that two high-frequency variants must co-occur in an appreciable fraction of cells (Text S3.1). This "pigeonhole principle" suggests that we can estimate the genotype of one of the lineages in a mixed sample by taking the major alleles present above some threshold frequency $f^* \gg 50\%$, and treating the remaining sites as missing data. Although the potential errors increase with the length of the inferred haplotype, we will not actually require genome-length haplotypes for our analysis here. Instead, we leverage the fact that significant evolutionary information is already encoded in the marginal distributions of one- and two-site haplotypes, so that these "quasi-phased" lineages will be sufficient for our present purposes.

The major challenge with this approach is that we do not observe the true allele frequency directly, but must instead estimate it from a noisy sample of sequencing reads. This can lead to phasing errors when the true major allele is sampled at low frequency by chance and is assigned to the opposite lineage (Fig. S1). The probability of such "polarization" errors can vary dramatically depending on the sequencing coverage and the true frequency of the major allele (Text S3.2). Previous approaches based on consensus alleles [35, 37] can therefore induce an unknown number of errors that make it difficult to confidently detect a small number of evolutionary changes between samples.

In Text S3.3, we show that by explicitly modeling the sampling error process, the expected probability of a polarization error in our cohort can be bounded to be sufficiently low if we take $f^* = 80\%$, and if we restrict our attention to samples with sufficiently high coverage and sufficiently low rates of intermediate-frequency polymorphism. We will refer to these as *quasi-phaseable* (QP) samples. In the *B. vulgatus* example above, Figs. 1C,D are classified as quasi-phaseable, while Figs. 1A,B are not. Note that quasi-phaseability is separately defined for each species in a metagenomic sample, rather than for the sample as a whole. For simplicity, we will still refer to these species-sample combinations as QP samples, with the implicit understanding that they refer to a particular focal species.

In Fig. 1F, we plot the distribution of QP samples across the most prevalent gut bacterial species in our panel. The fraction of QP samples varies between species, ranging from $\sim 50\%$ in the case of *P. copri* to nearly 100% for *B. fragilis* [4], and it accounts for much of the variation in the average polymorphism rate (Fig. S3). Most individuals carry a mixture of QP and non-QP species (Fig. S4), which suggests that quasi-phaseability arises independently for each species in a sample, rather than for the sample as a whole. Thus, although many species-sample combinations are non-QP, in a cohort of a few hundred samples it is not uncommon to find ≥ 50 QP samples in many prevalent species, which yields ~ 3000 quasi-phased haplotypes when aggregated across the different species. Consistent with previous studies of the stability of personal microbiomes [31, 35, 49], a majority of the longitudinally sampled species maintain

their QP classification at both timepoints, though this pattern is not universal (Fig. S5). We will revisit the peculiar properties of this within-host lineage distribution in the Discussion. For the remainder of the analysis, we will take the distribution in Fig. 1F as given and focus on leveraging the QP samples to quantify the evolutionary changes that accumulate between lineages in different samples.

We investigate two types of evolutionary changes between lineages in different QP samples. The first class consists of single nucleotide differences, which are defined as SNVs that transition from allele frequencies $\leq 1 - f^*$ in one sample to $\geq f^*$ in another, with $f^* \approx 80\%$ as above (Fig. S1). These thresholds are chosen to ensure low genome-wide false positive rate given the typical coverage and allele frequency distributions among the QP samples in our panel (Text S3.4). The second class consists of differences in gene presence or absence, in which the relative copy number of a gene, c, transitions from a value below the threshold of detection ($c < 0.05$) to the range in which the majority of single-copy genes lie ($0.5 < c < 2$, see Fig. S6), or vica versa. These thresholds are chosen to ensure a low genome-wide false positive rate across the QP samples, given the typical variation in sequencing coverage along the genome (Text S3.5).

Note that these SNV and gene changes represent only a subset of the potential differences between lineages, since they neglect other evolutionary changes (e.g., indels, genome rearrangements, or changes in high copy number genes) that are more difficult to quantify in a metagenomic sample, as well as more subtle changes in allele frequency and gene copy number that do not reach our stringent detection thresholds. We will revisit these and other limitations in more detail in the Discussion.

Long-term evolution across hosts

By focusing on the QP samples for each species, we can measure genetic differences between lineages in different hosts, as well as within hosts over short time periods. Descriptive summaries of this variation have been reported elsewhere [31, 33–35, 37, 44]. Here, we aim to leverage these patterns (and the increased resolution of the QP samples) to quantify the evolutionary dynamics that operate within species of gut bacteria, both within and across hosts.

To interpret the within-host changes in an evolutionary context, it will be useful to first understand the structure of genetic variation between lineages in different hosts. This variation reflects the long-term population genetic forces that operate within each species, integrating over many rounds of colonization, growth, and dispersal. To investigate these forces, we first analyzed the average nucleotide divergence between different pairs of QP hosts. Since the different species in a given set of hosts will generally have different evolutionary histories, these genetic distances must be evaluated separately for each species.

Bacteroides vulgatus will again serve as a useful case study, since it has the largest number of QP hosts in our panel. Figure 2A shows a UPGMA dendrogram based on pairwise nucleotide divergence averaged across the core genome. In a panmictic, neutrally evolving population, we would expect these distances to be clustered around their average value, $d \approx 2\mu N_e$, where N_e is the effective population size for the across-host population [50]. In contrast, Fig. 2A shows striking differences in the degree of relatedness between different hosts: even at this coarse, core-genome-wide level, the genetic distances vary over several orders of magnitude. Similarly broad ranges of divergence are observed in many other prevalent species as well (Figs. 2C and 3A), particularly in the *Bacteroides* genus.

The upper range of divergence values in *B. vulgatus*, as well as in a handful of other cases, are likely driven by genetically isolated "subspecies" [36]. These cases can be identified by the small fraction of SNVs that are shared across the top-level clades in the UPGMA dendrogram (Fig. 2B, Appendix S4 Text). Although the presence of subspecies is not universal, their occasional appearance at high divergence rates ($> 1\%$) is anticipated given the limitations of our reference-based species definition.

The more surprising features of Figs. 2 and 3 are the many pairs of lineages with extremely

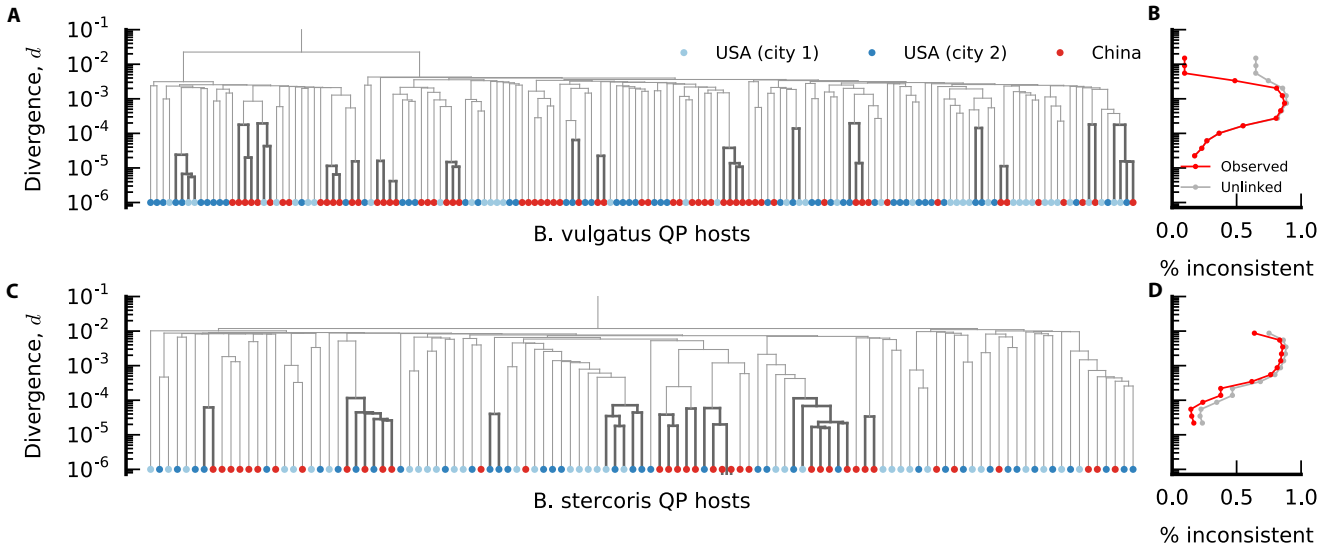

Fig 2. Genetic divergence between hosts in two *Bacteroides* species. (a) Dendrogram constructed from the average nucleotide divergence across the core genome of *B. vulgatus* in different pairs of QP hosts, based on UPGMA clustering (SI Section S4 Text). The underlying distribution of distances and their corresponding uncertainties are shown in Fig. S7. Each host is colored according to its geographic location. Branches with anomalously short divergence rates ($d < 2 \times 10^{-4}$) are highlighted in bold. (b) The fraction of phylogenetically inconsistent SNPs as a function of divergence (Text S4.2). The observed values are shown in red, while the expectations assuming independence between loci ('unlinked loci') are shown in grey for comparison. (c,d) Analgous versions of (a) and (b) for *Bacteroides stercoris*.

low divergence (e.g. $\lesssim 0.01\%$), which fall more than an order of magnitude below the typical between-host value even after correcting for subspecies structure. Isolated examples of such closely related strains have also been reported by Ref. [35], though their evolutionary interpretation remains unclear.

In principle, closely related strains can arise naturally in a large sample when two cells are sampled from the same clonal expansion (a breakdown of random sampling). However, such simple explanations are unlikely to apply here. Not only are the lineages sampled from different hosts, but we can also find pairs of closely related strains in Figs. 2A,C from different U.S. cities or different continents. More importantly, by leveraging information across multiple species, we find that pairs of hosts with closely related strains in one species are not any more likely have closely related strains in their other species (Fig. 3B). This allows us to rule out all other host-specific sampling biases that might be driven by unobserved factors.

Though the the rates of nucleotide divergence between these sister lineages are small, they are still significantly larger than the estimated false positive rate (Text S3.4), so the core genomes are genetically distinct. In addition, the closely related strains differ substantially in their gene content, with ~ 100 gene differences separating the two lineages (Fig. 3C). This suggests that the closely related strains represent a true intermediate genealogical timescale in bacterial population genetics, whose cause is yet unknown. This hypothesis is bolstered by the large number of prevalent species in Fig. 3A with anomalously low divergence rates between some pairs of hosts. However, we note that this pattern is not universal: some genera, like *Alistipes* or *Eubacterium*, show more uniform rates of divergence between hosts. Apart from these phylogenetic correlations, there are no obvious explanations for why some species have low divergence host pairs and others do not [e.g., sample size, abundance, vertical transmissibility [33], sporulation score [51]].

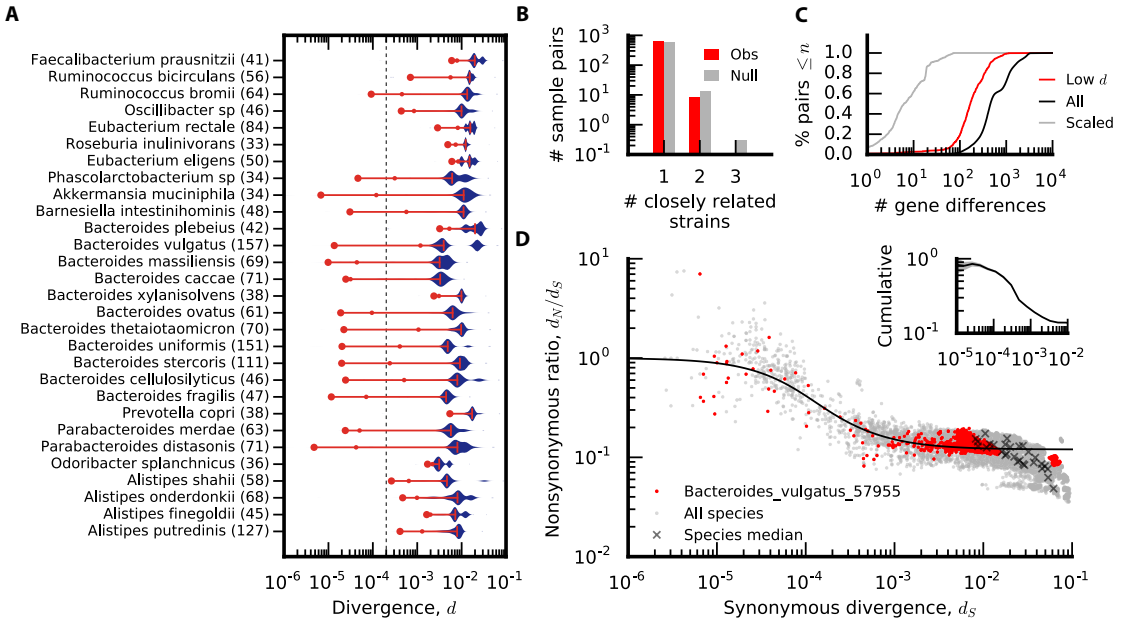

Fig 3. Between-host divergence across prevalent species of gut bacteria. (a) Distribution of average nucleotide divergence across the core genome between pairs of QP hosts (blue) for a panel of prevalent species. Species are sorted according to their phylogenetic distances [33], with the number of QP hosts indicated in parentheses; species were only included if they had at least 33 QP hosts (> 500 QP pairs). Symbols denote the median (dash), 1-percentile (small circle), and 0.1-percentile (large circle) of each distribution, and are connected by a red line for visualization; for distributions with $< 10^3$ data points, the 0.1-percentile is estimated by the second-lowest value. The dashed line denotes our ad-hoc definition of "closely related" divergence, $d \leq 2 \times 10^{-4}$. (b) The distribution of the number of species with closely related strains for each pair of hosts. The null distribution is obtained by randomly permuting hosts independently within each species ($n = 10^3$ permutations, $P \approx 0.9$). This shows that there is no tendency for the same pairs of hosts to have more closely related strains than expected under the null distribution above. (c) The cumulative distribution of the number of gene content differences for all pairs in panel A (black line), i.e., all choices of species x host 1 x host 2. The red line shows the corresponding distribution for the subset of closely related strains. For comparison, the grey line denotes a 'clock-like' null distribution for the closely related strains, which assumes that genes and SNVs each accumulate at constant rates. (d) Ratio of divergence at nondegenerate nonsynonymous sites (d_N) and fourfold degenerate synonymous sites (d_S) as a function of d_S for all pairs in panel A (grey circles). Pairs from *B. vulgatus* are highlighted in red for comparison. Crosses (x) denote species-wide estimates obtained from the ratio of the median d_N and d_S within each species. The black line denotes the theoretical prediction from the purifying selection null model in SI Section S5 Text. (inset) Ratio between the cumulative d_N and d_S values for all QP host pairs with core-genome-wide synonymous divergence less than d_S. The narrow shaded region denotes ±2 standard deviation confidence intervals estimated by Poisson resampling, which shows that $d_N/d_S \lesssim 1$ even for low d_S.

Different patterns of natural selection on short timescales

Given the existence of anomalously low divergence rates, we next asked whether natural selection behaves differently for mutations that accumulate on these shorter timescales, compared to the typical divergence rates between lineages. We focused on a common coarse-grained measure of natural selection by comparing the relative contribution of synonymous and nonsynonymous mutations that comprise the overall divergence rates in Fig. 3A. Specifically, we focused on the ratio between the per-site divergence at nonsynonymous sites (d_N) and the corresponding value at synonymous sites (d_S). Under the assumption that synonymous mutations are effectively neutral, the ratio d_N/d_S measures the average action of natural selection on mutations at nonsynonymous sites.

In Fig. 3D, we plot the distribution of d_N/d_S across every pair of QP hosts in each of the prevalent species in Fig. 3A. The values of d_N/d_S are plotted as a function of d_S (a proxy for the average divergence time across the genome). We observe a consistent negative relationship between these two quantities across the prevalent species in Fig. 3.

For large divergence times ($d_S \sim 1\%$), we observe only a small fraction of nonsynonymous mutations ($d_N/d_S \sim 0.1$), indicating widespread purifying selection on amino-acid replacements [31]. Yet among more closely related strains, we observe a much higher fraction of nonsynonymous changes, with d_N/d_S approaching unity when $d_S \sim 0.01\%$. Moreover, this negative relationship between d_N/d_S and d_S is much more pronounced than the variation in the typical values of d_N/d_S within different species (black crosses in Fig. 3D). While between-species variation may be driven by mutational biases, the strong within-species signal indicates that there are consistent differences in the action of natural selection as a function of time. This provides further support for the hypothesis that anomalously low values of d_S arise from a separate genealogical process.

The trend in Fig. 3D is consistent with a simple null model in which purifying selection is less efficient at purging deleterious variants on shorter timescales (SI Section S5 Text). In particular, we can reproduce the quantitative shape of Fig. 3D with a simple distribution of fitness effects, in which 90% of nonsynonymous variants have fitness costs on the order of $s/\mu \sim 10^5$, with the remaining sites being neutral. However, while this is the simplest possible null model that can explain the data, we cannot exclude more elaborate explanations for this trend, like enhanced adaptation and hitchhiking on short timescales, or a recent global shift in selection pressures caused by host-specific factors (e.g., the introduction of agriculture).

Quasi-sexual evolution on intermediate timescales

In principle, genome-wide patterns of divergence similar to Figs. 2 and 3 could arise in a model with strong population structure, in which all but the most closely related strains are genetically isolated from each other [52]. However, while this model may apply to the most deeply-diverged clades in certain species (e.g. *B. vulgatus*), we will now show that such genetic isolation does not hold for intermediate divergence times that separate typical pairs of strains in different hosts.

Our first line of evidence derives from inconsistencies in the dendrograms in Figs. 2A,C. In both *Bacteroides* species, a substantial fraction of core-genome SNVs that segregate in intermediate-divergence clades are inconsistent with core-genome-wide dendrogram (i.e., they are also polymorphic outside the clade, see Text S4.2). Moreover, the fraction of inconsistent core-genome SNVs is nearly indistinguishable from the expectation under a model of free recombination (Figs. 2B,D). Yet while this phylogenetic inconsistency is suggestive of recombination, it can also arise from purely clonal mechanisms (e.g., recurrent mutation), or from statistical uncertainties in the genome-wide tree.

We therefore sought additional evidence of recombination by examining the decay of linkage disequilibrium (LD) between pairs of synonymous SNVs in the core genome of each species. We quantified linkage disequilibrium using a standard [53] measure of gametic correlation, $\sigma_d^2 = \mathbb{E}[(f_{AB} - f_A f_B)^2]/\mathbb{E}[f_A(1-f_A)f_B(1-f_B)]$, with an unbiased estimator to control for varying sample size (SI Section S6 Text). The overall magnitude of σ_d^2 depends on various

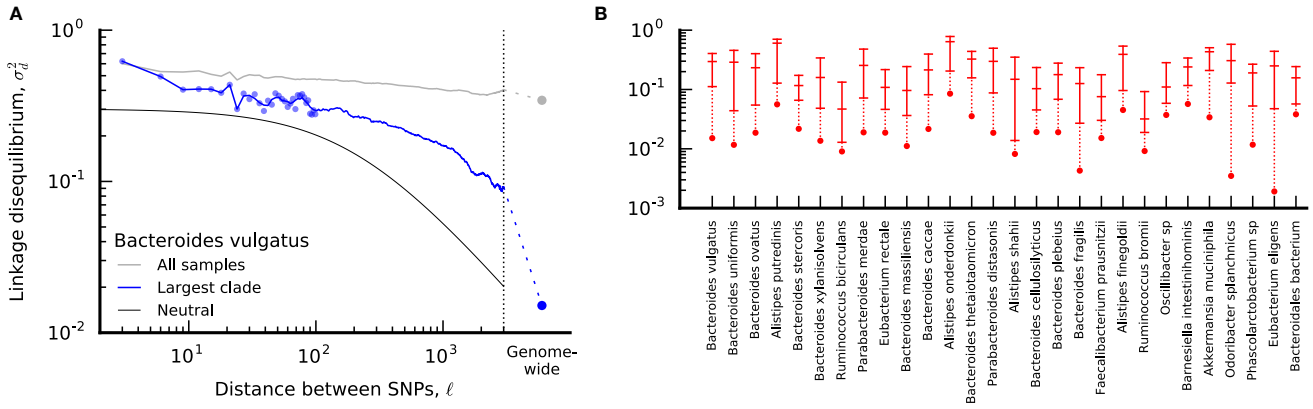

Fig 4. Decay of linkage disequilibrium at synonymous sites. (a) Linkage disequilibrium (σ_d^2) as a function of distance (ℓ) between pairs of fourfold degenerate synonymous sites in the same core gene in *B. vulgatus* (see SI Section S6 Text). Individual data points are shown for distances < 100bp, while the solid line shows the average in sliding windows of 0.2 log units. The grey line indicates the values obtained without controlling for population structure, while the blue line is restricted to QP hosts in the largest top-level clade (Table S2). The solid black line denotes the neutral prediction from SI Section S6 Text; the two free parameters in this model are σ_d^2 and ℓ scaling factors, which are shifted to enhance visibility. For comparison, the core-genome-wide estimate for SNVs in different genes is depicted by the dashed line and circle. (b) Summary of linkage disequilibrium for QP hosts in the largest top-level clade (see SI Section S6 Text) for all species with ≥ 10 QP hosts. For each species, the three dashes denote the value of $\sigma_d^2(\ell)$ for intragenic distances of $\ell = 9$, 99, and 2001 bp, respectively, while the core-genome-wide values are depicted by circles. Points belonging to the same species are connected by vertical lines for visualization.

factors (e.g., demography), while changes in σ_d^2 between different pairs of loci reflect differences in the effective recombination rate [54]. By focusing on QP samples, we can estimate σ_d^2 between SNVs that are separated by more distance (along the reference genome) than a typical sequencing read. However, since the synteny of individual lineages may differ substantially from the reference genome, we only assigned coordinate distances (ℓ) to pairs of SNVs in the same gene, which are more likely (but not guaranteed) to be nearby in the genomes in other samples; all other pairs of SNVs are grouped together in a single category ("core-genome-wide"). We then estimated σ_d^2 as a function of ℓ for each of these distance categories (SI Section S6 Text), and analyzed the shape of this function.

As an example, Fig. 4A illustrates the estimated values of $\sigma^2(\ell)$ for *B. vulgatus*; summarized versions of this function are shown for the other prevalent species in Fig. 4B. In almost all cases, we find that core-genome-wide LD is significantly lower than for pairs of SNVs in the same core gene, suggesting that much of the phylogenetic inconsistency in Fig. 2 is caused by recombination. In principle, this intergenic recombination could be driven by the exchange of operons or other large clusters of genes (e.g. on an extra-chromosomal plasmid). However, we also observe a significant decay in LD within individual genes (Fig. 4), suggesting a role for homologous recombination as well.

The magnitude of the decay of LD within core genes is somewhat less than has been observed in other bacterial species [16], and only rarely decays to genome-wide levels by the end of a typical gene. Moreover, by visualizing the data on a logarithmic scale, we see that the shape of $\sigma_d^2(\ell)$ is inconsistent with the predictions of the neutral model (Fig. 4A), decaying much more slowly with ℓ than the $\sim 1/\ell$ dependence expected at large distances [53]. Thus, while we can obtain rough estimates of r/μ by fitting the data to a neutral model (which generally support $0.1 \lesssim r/\mu \lesssim 10$, see Fig. S9), these estimates should be regarded with caution because they vary depending on the length scale on which they are measured (SI Section S6 Text). This suggests that new theoretical models will be required to fully understand the patterns of recombination that we observe. In either case, the widespread evidence for recombination makes the closely related

lineages in Figs. 2 and 3 even more surprising, since they require strong correlations between a large number of otherwise independent loci. We will revisit these apparent breakdowns of quasi-sexuality again in the Discussion.

Short-term succession within hosts

In the previous sections, we focused on longer-term evolutionary changes that accumulate over many host colonization cycles. However, one of the main advantages of our quasi phasing method is that it can be used to investigate short-term changes within hosts as well. Previous studies of longitudinally sampled metagenomes have shown that on average, two samples from the same host are more similar to each other than to samples from different hosts [31, 33, 35, 44, 55, 56]. This suggests that resident sub-populations of bacteria often persist within hosts for $\gtrsim 1$ year ($\sim 300 - 3000$ generations), potentially enough time for evolutionary adaptation to occur [7]. However, the limited resolution of previous metagenome-wide [31] or species-averaged [35, 44] comparisons has made it difficult to quantify the individual changes that accumulate between lineages on these short timescales, and to interpret these changes in an evolutionary context.

To address this issue, we focused on the subset of species in longitudinally sampled individuals that were quasi-phaseable at consecutive timepoints. For these samples, we show that the estimated false positive rates are sufficiently low that we expect to resolve a single nucleotide difference between the two timepoints in a genome-wide scan (Text S3.4). To boost sensitivity, we considered SNVs in both core and accessory genes, since the latter might be expected to be enriched for short-term targets of selection [57].

To build intuition for these data, we will begin by using *B. vulgatus* as a case study, and will later expand our analysis to ~ 30 of the most prevalent species in our panel. Figure 5A shows the distribution of the total number of nucleotide differences between timepoints in *Bacteroides vulgatus*; the median number of between-host differences, as well as the 50 lowest values, are also included for comparison. Consistent with previous work, the number of within-host differences are typically much smaller than the differences that are observed between hosts. However, in a few rare cases, pairs of consecutive timepoints possess more than 1000 substitutions, which is well within the bounds of the between-host distribution. This likely indicates a replacement event, in which the primary resident lineage is succeeded by an unrelated lineage from the larger metapopulation. Among the remaining individuals, we observe either zero nucleotide differences between the two timepoints, or a much smaller number of changes, consistent with an evolutionary modification of an existing lineage. Given the large census population sizes in the gut, we conclude that these rapid allele frequency changes must be driven by natural selection, rather than genetic drift. However, this does not imply that the observed SNVs are the direct target of selection: given the limitations of our reference-based approach, the observed mutations may simply be passengers hitchhiking alongside an unseen selected locus. In either case, given the frequency change and the length of the sampling period, we infer that the selected haplotype must have had a fitness benefit of at least $S \sim 1\%$ per day at some point during the sampling window.

There are only a small number of SNV modifications in the example in Fig. 5, which makes it difficult to tell whether these changes reflect selection on *de novo* mutations or introgression from other species or lineages [58]. We can gain more insight into this question by investigating the gene content differences between timepoints (Fig. 5B,C). As for SNV changes above, the estimated false positive rates for QP samples are sufficiently low that we expect to resolve a single gene gain or loss in a pangenome-wide scan (Text S3.5). The gene losses in Fig. 5B could have been generated by mutations (e.g. large deletion events) or by horizontal exchange (e.g. recombination with a homologous fragment where the genes have already been deleted). By contrast, the gene gains in Fig. 5C must be pre-existing variants, likely acquired through recombination with another lineage.

Compared to the SNV distribution in Fig. 5A, more of the individuals show evidence for at

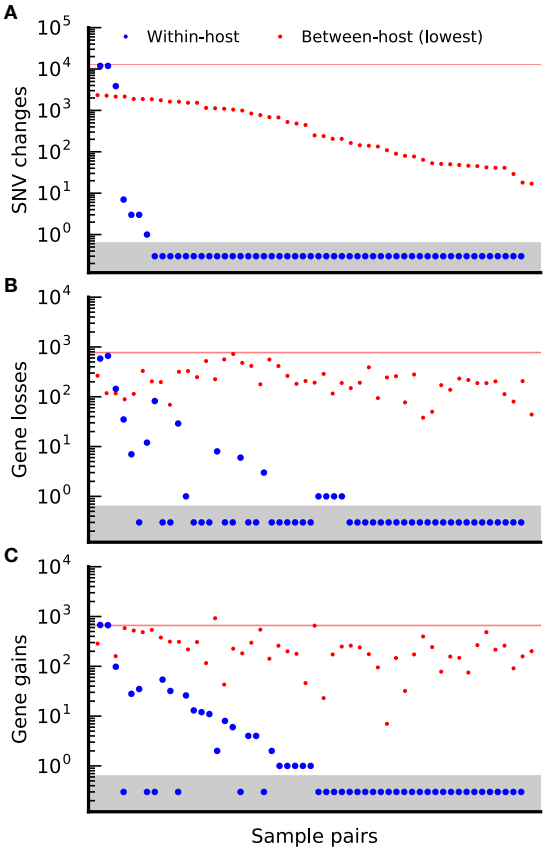

Fig 5. Within-host changes in *Bacteroides vulgatus*. (a) Number of detected nucleotide differences in core and accessory genes between pairs of QP samples from the same host at two consecutive timepoints (blue circles). Samples with zero detected changes are assigned an arbitrary value < 1 (grey region) so that they can be visualized on the logarithmic scale. Samples are sorted in descending order, with ties broken by the total number of gene changes in panels (b) and (c) described below. For comparison, the 50 lowest values from the between-host distribution (red points) and the median between-host value (solid red line) are shown. (b,c) the number of gene losses (b) and gains (c) for the samples in (a), in the same order as (a). The dashed line again denotes the median between-host value in both cases, while the red points show the corresponding gene losses (b) and gains (c) for the between-host comparisons in (a), in the same order as (a).

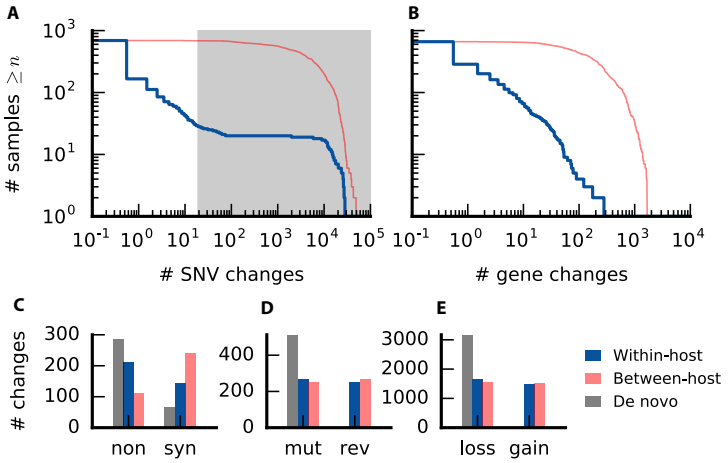

Fig 6. Within-host changes across prevalent species of gut bacteria. (a) Within-host nucleotide differences over ~ 6 months. The blue line shows the distribution of the number of SNV differences between consecutive timepoints for different species and hosts; species are only included if they have ≥ 5 hosts with consecutive QP timepoints, and samples with zero changes are assigned an arbitrary value < 1 so that they can be visualized on the logarithmic scale. For comparison, the red line shows the distribution of the minimum number of SNV differences between each host and the other hosts in our panel. The grey region indicates an ad-hoc threshold used to define replacement events in panels (b-e), chosen to be conservative in calling non-replacements. (b) Within-host gene content differences (gains+losses) in non-replacement timepoints. The blue line shows the distribution of the number of gene content differences for the samples in (a), excluding those in the grey region. As in (a), an analogous between-host distribution is shown for comparison. (c) The total number of nucleotide differences at non-degenerate nonsynonymous sites (non) and fourfold degenerate synonymous sites (syn) for the non-replacement samples (a), illustrated in blue. For comparison, we have also included the expected distribution of *de novo* mutations (randomly selected sites, grey) and between-host differences (red), conditioned on the same total number of events. (d) The total number of nucleotide differences that transition away from the panel-wide consensus allele (mut) and back toward the consensus allele (rev) for the non-replacement species-host combinations in (a). Between-host and *de novo* expectations are the same as in (c). (e) The total number of gene loss and gain events among the gene content differences in (b). The between-host expectation is the same as in (d), while the *de novo* expectation is only losses.

least one gene difference in Figs. 5B,C, and the average number of differences per individual is slightly higher. The genes that are gained and lost tend to be drawn from the accessory portion of the *B. vulgatus* genome (present in $\leq 90\%$ of samples) (Fig. S11A), consistent with the expectation that these genes are more likely to be gained or lost over time. Within a single host, gene changes tend to be spatially clustered along the reference genome in which they are found, suggesting that multiple genes may be altered in a single gene-change event (Fig. S11B). Similar patterns are observed in sequenced isolates [59] and metagenomes from different hosts [55]. Thus, the number of introgression events may be significantly lower than the number of gene changes in Figs. 5B,C.

Although we have focused on *B. vulgatus* as an example, the general patterns in Fig. 5 are recapitulated in many other prevalent species as well (Fig. S12). We can therefore gain more information about the tempo and mode of adaptation by pooling within-host changes across different species and hosts (Fig. 6). In this larger sample, we see that outright replacement events are relatively rare over the ~ 6 month sampling window ($\approx 5\%$ of host-species pairs), though they would dominate the average number of within-host SNV differences if we did not exclude them (Fig. 6A). Below this replacement threshold, $\approx 20\%$ of host-species pairs acquire a modest number of SNV modifications between the two timepoints. These SNV differences are evenly split between "mutations" away from the consensus allele across the panel, or "reversions" back toward it (Fig. 6D). The proportion of reversions is significantly higher than expected for a randomly selected site, and is closer to the distribution of between-host differences. In addition, there are fewer nonsynonymous mutations within hosts than one would expect for neutral or positively-selected sites ($dN/dS \approx 0.4$, Fig. 6C). Instead, the fraction of nonsynonymous mutations is shifted towards the between-host distribution in Fig. 3D, even though we expect few deleterious mutations to be efficiently purged on ~ 6 month timescales. The excess of SNV reversions and low d_N/d_S, combined with the high fraction of gene gains in Fig. 6E, suggest that many of these SNV differences are likely acquired via introgression from another species or strains. In this case, natural selection could have had more time to purge deleterious variants on the introgressed fragment, resulting in the lower fraction of nonsynonymous mutations observed in Fig. 3D. Although lower than expected for *de novo* mutations, the fraction of nonsynonymous mutations is still slightly higher than in a typical between-host comparison. These extra nonsynonymous mutations could be consistent with a small fraction of *de novo* driver or passenger mutations, as well as a preference toward introgression from more closely related strains.

In the pooled data, gene changes are again more prevalent than SNV changes, with $\sim 30\%$ of host-species pairs showing some gene-content differences between timepoints (Fig. 6B). Many of these genes are annotated as transposons, integrases, transferases, and mobilization proteins (Table S3), consistent with the hypothesis that they originated through recombination. Similar conjugative elements have been associated with transfers between different *Bacteroidales* species that colonize the same host [59]. We also observe a handful of gene changes in other functional categories (e.g. transcriptional regulators, transmembrane proteins, and ABC transporters). Similar categories are found for genes that harbor SNV differences over time (Table S4). However, in both cases the vast majority of affected genes remain unannotated. Further investigation of the functional parallelism of within-host changes remains an interesting avenue for future work.

Discussion

Evolutionary processes can play an important role in many microbial communities. Yet despite increasing amounts of sequence data, our understanding of these processes is often limited by our ability to resolve evolutionary changes in populations from complex communities. In this work, we quantify the evolutionary forces that operate within bacteria in the human gut microbiome, based on a more detailed characterization of the lineage structure in metagenomic samples from individual hosts.

Building on previous work by Ref. [35] and others, we found that the lineage structure in many prevalent species is consistent with colonization by a few distinct strains from the larger population, with the identities and frequencies of these strains varying from person to person (Fig. 1). The distribution of strain frequencies in this "oligo-colonization model" is itself quite interesting: in the absence of fine tuning, it is not clear what mechanisms would allow for a second or third strain to reach intermediate frequency, while preventing a large number of other lineages from entering at the same time. A better understanding of the colonization process, and how it might vary among the species in Fig. 1F, is an important avenue for future work.

Given the wide variation among species and hosts, we chose to focus on a subset of samples with particularly simple strain mixtures for a given species, in which we can resolve evolutionary changes in the dominant lineage with a high degree of confidence. Our quasi-phasing approach can be viewed as a refinement of the consensus approximation employed in earlier studies [4, 35, 37, 38], but with more quantitative estimates of the errors associated with detecting genetic differences between lineages in different samples.

By analyzing genetic differences between lineages in separate hosts, we found that long-term evolutionary dynamics in many gut bacteria are consistent with quasi-sexual evolution and purifying selection, with relatively weak geographic structure. Earlier work had documented extensive horizontal transfer between distantly related species in the gut [60, 61], but our ability to estimate rates of recombination within species was previously limited by the small number of sequenced isolates for many species of gut bacteria [62]. The high rates of homologous recombination we observed with our quasi-phasing approach are qualitatively consistent with previous observations in other bacterial species [16, 62–66]. However, our quantitative characterization of linkage disequilibrium revealed interesting departures from the standard neutral prediction that cannot be captured by simply lowering the recombination rate. Our results suggest that it would be interesting to see whether similar departures can be detected in the previously studied species above, or whether these altered signatures of recombination are unique to the prevalent species of gut bacteria studied here.

In a complex community like the gut, a key advantage of our metagenomic approach is that it allows us to jointly measure genetic differences in multiple species for the same pair of hosts. By leveraging this feature, we uncovered evidence for additional genealogical processes operating at very short timescales between hosts (Fig. 3B), with altered signatures of selection (Fig. 3D) and potentially recombination as well (Fig. S10). Given the homogenizing effects of recombination above, it is difficult to produce such a broad range of core-genome-wide divergence in traditional population genetic models, though recent hybrid models of vertical and horizontal inheritance could potentially provide an explanation for this effect [66, 67]. Our findings suggest that this may be an interesting signature to explore in future theoretical work, in addition to further empirical characterization in larger cohorts and over shorter genomic distances. In either case, our results suggest that the short-term dynamics of across-host evolution may not be easily extrapolated by comparing sequences of typical isolates.

The other main advantage of our quasi-phasing approach is its ability to resolve a small number of evolutionary changes that could accumulate within hosts over short timescales. Previous work has shown that on average, longitudinally sampled metagenomes from the same host are more similar to each other than metagenomes from different hosts [31, 33, 35, 44, 55, 56]. However, the limited resolution of these metagenome-wide [31] or species-averaged [35, 44] comparisons has made it difficult to distinguish true within-host differences from sampling noise, and to ultimately interpret these changes in an evolutionary context. In contrast, our quasi-phasing approach enables more finely resolved estimates of temporal change within individual species in individual hosts. This shift is crucial, since our results show that metagenome- or species-averaged estimates of longitudinal variation arise from a mixture of two characteristic processes, which we term *replacement* and *modification*.

Consistent with previous work, we observed a small number of replacement events in which the dominant lineage is succeeded by a strain as distantly related as those in other hosts. In such

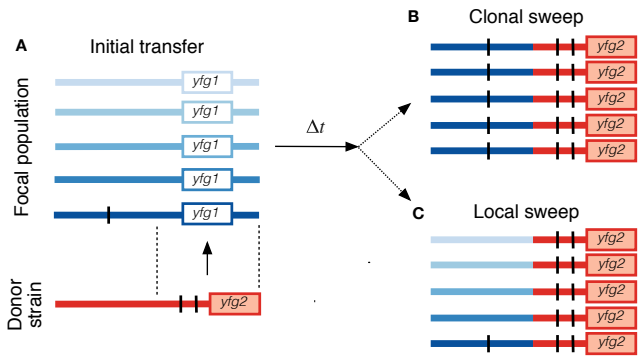

Fig 7. Putative model of within-host evolution. (a) A hypothetical introgression event, in which a new gene (*yfg2*) and two SNVs (black lines) are transferred from a donor strain (red) into a single individual in the focal population (blue, each individual is assigned a unique shade). In addition to the gene gain and SNV substitutions, this introgression event also results in the loss of the existing gene *yfg1* in the introgressed individual. (b) An example of a clonal sweep, in which the initial recombinant in (a) sweeps to fixation in the focal population, resulting in a within-host gene gain (*yfg2*), a gene loss (*yfg1*), and 3 SNV changes (2 on the introgressed fragement, 1 *de novo* variant). (c) An example of a clonal sweep, in which the introgressed fragment is able to recombine onto other genetic backgrounds before it reaches fixation. Note that the private variant (left most black line) no longer hitchhikes to fixation.

cases, a key question is whether the succeeding strains are newly acquired from the environment, or whether they reflect an earlier colonization event where the strain persists at low frequency. Although these scenarios are difficult to distinguish from our present data, they could potentially be distinguished in longer and more densely sampled time series, since a preexisting lineage could re-emerge in later timepoints [25]. One such reversal occurred in *B. vulgatus* within an individual sampled at three timepoints (Fig. S13A), which provides some anecdotal support for the pre-existing strains hypothesis.

In addition to these rare replacement events, we more commonly observed lineages that differed by only a handful of SNV and gene changes, consistent with an evolutionary modification of the resident strain. This broad range of outcomes shows why it is essential to understand the distribution of temporal variation across hosts: even though modification events are more common than replacements, their signal is quickly diluted in species- or metagenome-wide averages as soon as a few replacements are present. As a result, we expect that previous estimates of longitudinal variation largely reflect the rates and genetic differences associated with replacement events, rather than evolutionary change. Although the modification events could also theoretically arise via replacement by an extremely closely related strain, our results suggest that this scenario is less likely, since it requires circulating strains that are more closely related than even the lower tail of the between-host distribution (Fig. 5), and with a smaller fraction of nonsynonymous differences than we expect for such closely related strains (Fig. 3D). However, unambiguous proof of evolution could be observed in a longer timecourse, since subsequent modifications should eventually accumulate in the background of earlier substitutions. Even in our limited data, we can already observe a few examples of this behavior in individuals sampled at three timepoints (Fig. S13B,C), which provides further support for the evolutionary hypothesis.

Many of the mutations we observed were gene gain events, which, combined with the signatures of the sweeping SNVs (Fig. 6), suggests that SNV and gene modifications are often acquired via introgression from an existing strain (illustrated in Fig. 7A). This stands in contrast to the *de novo* mutations observed in microbial evolution experiments [13] and some within-host pathogens [21, 22]. Yet in hindsight, it is easy to see why adaptive introgression could be a more efficient route to adaptation in a complex ecosystem like the gut microbiome, given the large strain diversity [42], the high rates of DNA exchange [60, 61], and the potentially larger selective advantage of importing an existing functional unit [11]. Consistent with this hypothesis, adaptive

introgression events have also been observed on slightly longer timescales in bacterial biofilms from an acid mine drainage system [14], and they are an important force in the evolution of virulence and antibiotic resistance in clinical settings [68].

While the data suggest that within-host sweeps are often initiated by a recombination event, it is less clear whether recombination is relevant during the sweep itself. Given the short timescales involved, and our estimates of the recombination rate (Fig. S9), we would expect many of the observed sweeps to proceed in an essentially clonal fashion (Fig. 7B), since recombination would have little time to break up a megabase-sized genome. If this were the case, it would provide many opportunities for substantially deleterious mutations (with fitness costs of order $S_d \sim 1\%$ per day) to hitchhike to high frequencies within hosts [69], thereby limiting the ability of bacteria to optimize to their local environment. The typical fitness costs inferred from Fig. 3D lie far below this threshold, and would therefore be difficult to purge within individual hosts. In this scenario, the low values of d_N/d_S observed between hosts (as well as the putative introgression events) would crucially rely on the competition process across hosts [70].

Although the baseline recombination rates suggest clonal sweeps, there are other vectors of exchange (e.g. transposons, prophage, etc.) with much higher rates of recombination. Such mechanisms could allow within-host sweeps to behave in a quasi-sexual fashion, preserving genetic diversity elsewhere in the genome (Fig. 7C). These "local" sweeps are occasionally observed in other bacterial systems [15, 17]. If local sweeps were also a common mode of adaptation in the gut microbiome, they would allow bacteria to purge deleterious mutations more efficiently than in the clonal scenario above. In principle, we can distinguish between clonal and local sweeps by searching for SNV substitutions in non-QP samples, and then checking whether diversity is maintained at other loci after the sweep. Although we must employ more stringent criteria to detect sweeps in these non-QP samples, we can find a few individual examples of putatively clonal and local behavior (Fig. S14, SI Section S7 Text). However, in the latter case, it is difficult to distinguish a true local sweep from a clonal event in a gene that is present in only one of the lineages in the host. In this case, we would require longer-range linkage information [41] to determine whether the sweeping alleles are present in multiple strains.

While we have identified many interesting signatures of within-host adaptation, there are several important limitations to our analysis. First, our reference-based approach only allows us to track SNVs and gene copy numbers in the genomes of previously sequenced isolates of a given species. Within this subset, we have also imposed a number of stringent bioinformatic filters, further limiting the sequence space that we consider. Thus, it is likely that we are missing many of the true targets of selection, which might be expected to be concentrated in the host-specific portion of the microbiome, multi-copy gene families, or in genes that are shared across multiple prevalent species. A second important limitation of our approach is that it can only identify complete or nearly complete sweeps within individual hosts. While we observed many within-host changes that matched this criterion, we may be missing many other examples of within-host adaptation where variants do not completely fix. Given the large population sizes involved, such sweeps can naturally arise from phenotypically identical mutations at multiple genetic loci [71, 72], or through additional ecological partitioning between the lineages of a given species [25]. Both mechanisms have been observed in experimental populations of *E. coli* adapting to a model mouse microbiome [7].

Two concurrent studies have also documented short-term evolution of gut bacteria within healthy human hosts [73, 74]. In contrast to our metagenomic approach, each of these studies sequenced a large number of clonal isolates from a single bacterial species, *E. coli* in Ref. [73] and *B. fragilis* in Ref. [74]. Although *E. coli* was not sufficiently abundant in our cohort to be included in our analysis, the observations in *B. fragilis* are largely consistent with our findings that within-host evolution can be rapid, and that it can proceed via adaptive introgression. Crucially, since these observations were obtained using an isolate-based approach, they are not subject to the same methodological limitations described above, and they therefore serve as an independent verification of our results. However, since our statistical approach provides simultaneous

observations across more than ∼ 30 prevalent species, our results show that these general patterns of within-host evolution are shared across many species of gut bacteria, and they demonstrate a general approach for investigating these forces in widely available metagenomic data. Future efforts to combine metagenomic- and isolate-based approaches, e.g. by incorporating long-range linkage information [41, 75, 76], will be crucial for building a more detailed understanding of these evolutionary processes.

Acknowledgments

We thank S. Wyman for assistance with sample metadata and S. Greenblum, S. Venkataram, A. Harpak, J. Ladau, I. Cvijović, and members of the Pollard and Hallatschek labs for feedback. This research was supported in part by the National Science Foundation (PHY-1125915 and DMS-1563159), the National Institutes for Health (R25GM067110), and the Gordon and Betty More Foundation (No. 2919.01). BHG acknowledges support from the Miller Institute for Basic Research in Science at the University of California Berkeley. OH acknowledges support from a National Science Foundation Career Award (No. 1555330) and a Simons Investigator award from the Simons Foundation (No. 327934). KSP acknowledges support from Gladstone Institutes, Chan-Zuckerberg Biohub, and the San Simeon Fund.

References

1. David LA, Maurice CF, Carmody RN, Gootenberg DB, et al. Diet rapidly and reproducibly alters the human gut microbiome. Nature. 2013;505:559–563.

2. Seedorf H, Griffin NW, Ridaura VK, Reyes A, et al. Bacteria from Diverse Habitats Colonize and Compete in the Mouse Gut. Cell. 2014;159:253–266.

3. Rakoff-Nahoum S, Foster KR, Comstock LE. The evolution of cooperation within the gut microbiota. Nature. 2016;533:255–259.

4. Verster AJ, Ross BD, Radey MC, Bao Y, et al. The Landscape of Type VI Secretion across Human Gut Microbiomes Reveals Its Role in Community Composition. Cell Host & Microbe. 2017;22:411–419.

5. Bradley PH, Nayfach S, Pollard KS. Phylogeny-corrected identification of microbial gene families relevant to human gut colonization. biorXiv. 2017;.

6. Matamouros S, Hayden HS, Hager KR, Brittnacher MJ, Lachance K, Weiss EJ, et al. Adaptation of commensal proliferating Escherichia coli to the intestinal tract of young children with cystic fibrosis. Proceedings of the National Academy of Sciences. 2018; p. 201714373.

7. Barroso-Batista J, Sousa A, Lourenço M, Bergman ML, Sobral D, Demengeot J, et al. The first steps of adaptation of Escherichia coli to the gut are dominated by soft sweeps. PLoS genetics. 2014;10(3):e1004182.

8. Barroso-Batista J, Demengeot J, Gordo I. Adaptive immunity increases the pace and predictability of evolutionary change in commensal gut bacteria. Nature Communications. 2015;6:8945.

9. Lescat M, Launay A, Ghalayini M, Magnan M, Glodt J, Pintard C, et al. Using long-term experimental evolution to uncover the patterns and determinants of molecular evolution of an Escherichia coli natural isolate in the streptomycin-treated mouse gut. Molecular ecology. 2017;26(7):1802–1817.

10. Goodman AL, McNulty NP, Zhao Y, Leip D, et al. Identifying Genetic Determinants Needed to Establish a Human Gut Symbiont in Its Habitat. Cell Host & Microbe. 2009;6:279–289.

11. Wu M, McNulty NP, Rodionov DA, Khoroshkin MS, et al. Genetic determinants of in vivo fitness and diet responsiveness in multiple human gut Bacteroides. Science. 2015;350:aac5992.

12. Didelot X, Walker AS, Peto TE, Crook DW, Wilson DJ. Within-host evolution of bacterial pathogens. Nat Rev Microbiol. 2016;14:150–162.

13. Jerison ER, Desai MM. Genomic investigations of evolutionary dynamics and epistasis in microbial evolution experiments. Current Opinion in Genetics & Development. 2015;35:33–39.

14. Denef VJ, Banfield JF. In Situ Evolutionary Rate Measurements Show Ecological Success of Recently Emerged Bacterial Hybrids. Science. 2012;336:462–466.

15. Shapiro BJ, Friedman J, Cordero OX, Preheim SP, et al. Population genomics of early events in the ecological differentiation of bacteria. Science. 2012;336:48–51.

16. Rosen MJ, Davison M, Bhaya D, Fisher DS. Fine-scale diversity and extensive recombination in a quasisexual bacterial population occupying a broad niche. Science. 2015;348:1019–1023.

17. Bendall ML, Stevens SLR, Chan LK, Malfatti S, et al. Genome-wide selective sweeps and gene-specific sweeps in natural bacterial populations. The ISME Journal. 2016;10:1589–1601.

18. Herron MD, Doebeli M. Parallel Evolutionary Dynamics of Adaptive Diversification in *Escherichia coli*. PLoS Biology. 2013;11:e1001490.

19. Lang GI, Rice DP, Hickman MJ, Sodergren E, Weinstock GM, Botstein D, et al. Pervasive genetic hitchhiking and clonal interference in forty evolving yeast populations. Nature. 2013;500:571–574.

20. Tenaillon O, Barrick JE, Ribeck N, Deatherage DE, Blanchard JL, et al. Tempo and mode of genome evolution in a 50,000-generation experiment. Nature. 2016;536:165–170.

21. Lieberman TD, Flett KB, Yelin I, Martin TR, McAdam AJ, Priebe GP, et al. Genetic variation of a bacterial pathogen within individuals with cystic fibrosis provides a record of selective pressures. Nature Genetics. 2014;46:82–87.

22. Zanini F, Brodin J, Thebo L, Lanz C, Bratt G, Albert J, et al. Population genomics of intrapatient HIV-1 evolution. eLife. 2015;4:e11282.

23. Traverse CC, Mayo-Smith LM, Poltak SR, Cooper VS. Tangled bank of experimentally evolved Burkholderia biofilms reflects selection during chronic infections. Proc Natl Acad Sci USA. 2013;110:E250–E259.

24. Xue KS, Stevens-Ayers T, Angela P, Campbell JA, et al. Parallel evolution of influenza across multiple spatiotemporal scales. eLife. 2017;6:e26875.

25. Good BH, McDonald MJ, Barrick JE, Lenski RE, Desai MM. The dynamics of molecular evolution over 60,000 generations. Nature. 2017; p. in press.

26. Moeller AH, Caro-Quintero A, Mjungu D, Georgiev AV, et al. Cospeciation of gut microbiota with hominids. Science. 2016;353:380–382.

27. Tikhonov M, Monasson R. A collective phase in resource competition in a highly diverse ecosystem. Phys Rev Lett. 2017;118:048103.

28. Taillefumier T, Posfai A, Meir Y, Wingreen NS. Microbial consortia at steady supply. eLife. 2017;6:e22644.

29. Koskella B, Hall LJ, Metcalf CJE. The microbiome beyond the horizon of ecological and evolutionary theory. Nat Ecol Evol. 2017;1(11):1606–1615. doi:10.1038/s41559-017-0340-2.

30. Tikhonov M, Leach RW, Wingreen NS. Interpreting 16S metagenomic data without clustering to achieve sub-OTU resolution. The ISME journal. 2015;9(1):68.

31. Schloissnig S, Arumugam M, Sunagawa S, Mitreva M, Tap J, Zhu A, et al. Genomic variation landscape of the human gut microbiome. Nature. 2013;493:45–50.

32. Segata N, Waldron L, Ballarini A, Narasimhan V, Jousson O, Huttenhower C. Metagenomic microbial community profiling using unique clade-specific marker genes. Nature methods. 2012;9(8):811.

33. Nayfach S, Rodriguez-Mueller B, Garud N, Pollard KS. An integrated metagenomics pipeline for strain profiling reveals novel patterns of bacterial transmission and biogeography. Genome Res. 2016;26:1612–1625.

34. Scholz M, Ward DV, Pasolli E, Tolio T, Zolfo M, Asnicar F, et al. Strain-level microbial epidemiology and population genomics from shotgun metagenomics. Nature methods. 2016;13(5):435.

35. Truong DT, Tett A, Pasolli E, Huttenhower C, Segata N. Microbial strain-level population structure and genetic diversity from metagenomes. Genome Res. 2017;27:626–638.

36. Costea PI, Coelho LP, Sunagawa S, Munch R, Huerta-Cepas J, Forslund K, et al. Subspecies in the global human gut microbiome. Mol Syst Biol. 2017;13(12):960. doi:10.15252/msb.20177589.

37. Nayfach S, Pollard KS. Population genetic analyses of metagenomes reveal extensive strain-level variation in prevalent human-associated bacteria. bioRxiv. 2015;.

38. Zolfo M, Tett A, Jousson O, Donati C, Segata N. MetaMLST: multi-locus strain-level bacterial typing from metagenomic samples. Nucleic Acids Res. 2017;45(2):e7.

39. Luo C, Knight R, Siljander H, Knip M, et al. ConStrains identifies microbial strains in metagenomic datasets. Nat Biotechnol. 2015;33:1045–52.

40. Smillie CS, Sauk J, Gevers D, Friedman J, Sung J, Youngster I, et al. Strain Tracking Reveals the Determinants of Bacterial Engraftment in the Human Gut Following Fecal Microbiota Transplantation. Cell Host & Microbe. 2018;23(2):229–240.

41. Kuleshov V, Jiang C, Zhou W, Jahanbani F, Batzoglou S, Snyder M. Synthetic long-read sequencing reveals intraspecies diversity in the human microbiome. Nature Biotechnology. 2016;34(1):64–69.

42. Consortium HMP. A framework for human microbiome research. Nature. 2012;486:215–221.

43. Qin J, Li Y, Cai Z, Li S, et al. A metagenome-wide association study of gut microbiota in type 2 diabetes. Nature. 2012;490:55–60.

44. Lloyd-Price J, Mahurkar A, Rahnavard G, Crabtree J, et al. Strains, functions and dynamics in the expanded Human Microbiome Project. Nature. 2017;in press.

45. Sung W, Ackerman MS, Miller SF, Doak TG, Lynch M. Drift-barrier hypothesis and mutation-rate evolution. Proc Natl Acad Sci USA. 2012;109:18488–18492.

46. Poulsen LK, Licht TR, Rang C, Krogfelt KA, Molin S. Physiological state of *Escherichia coli* BJ4 growing in the large intestines of streptomycin-treated mice. J Bacteriol. 1995;177:5840–5845.

47. Russell SL, Cavanaugh CM. Intrahost Genetic Diversity of Bacterial Symbionts Exhibits Evidence of Mixed Infections and Recombinant Haplotypes. Molecular Biology and Evolution. 2017;msx188.

48. Olm MR, Brown CT, Brooks B, Firek B, et al. Identical bacterial populations colonize premature infant gut, skin, and oral microbiomes and exhibit different *in situ* growth rates. Genome Research. 2017;27:601–612.

49. Faith JJ, Guruge JL, Charbonneau M, Subramanian S, Seedorf H, Goodman AL, et al. The long-term stability of the human gut microbiota. Science. 2013;341(6141):1237439.

50. Wakeley J. Coalescent Theory, an Introduction. Greenwood Village, CO: Roberts and Company; 2009.

51. Browne HP, Forster SC, Anonye BO, Kumar N, Neville BA, Stares MD, et al. Culturing of 'unculturable' human microbiota reveals novel taxa and extensive sporulation. Nature. 2016;533(7604):543–546. doi:10.1038/nature17645.

52. Smith JM, Smith NH, O'Rourke M, Spratt BG. How clonal are bacteria? Proc Natl Acad Sci USA. 1993;90(10):4384–4388.

53. Ohta T, Kimura M. Linkage disequilibrium at steady state determined by random genetic drift and recurrent mutation. Genetics. 1969;63:229–238.

54. Slatkin M. Linkage disequilibrium – understanding the evolutionary past and mapping the medical future. Nature Reviews Genetics. 2008;9:477–485.

55. Zhu A, Sunagawa S, Mende DR, Bork P. Inter-individual differences in the gene content of human gut bacterial species. Genome Biol. 2015;16:82.

56. Voigt AY, Costea PI, Kultima JR, Li SS, Zeller G, Sunagawa S, et al. Temporal and technical variability of human gut metagenomes. Genome Biol. 2015;16:73. doi:10.1186/s13059-015-0639-8.

57. Greenblum S, Carr R, Borenstein E. Extensive strain-level copy-number variation across human gut microbiome species. Cell. 2015;160:583–94.

58. Hedrick PW. Adaptive introgression in animals: examples and comparison to new mutation and standing variation as sources of adaptive variation. Molecular Ecology. 2013;22:4606–4618.

59. Coyne MJ, Zitomersky NL, McGuire AM, Earl AM, Comstock LE. Evidence of extensive DNA transfer between bacteroidales species within the human gut. MBio. 2014;5(3):e01305–14. doi:10.1128/mBio.01305-14.

60. Smillie CS, Smith MB, Friedman J, Cordero OX, David LA, Alm EJ. Ecology drives a global network of gene exchange connecting the human microbiome. Nature. 2011;480(7376):241–4. doi:10.1038/nature10571.

61. Brito IL, Yilmaz S, Huang K, Xu L, Jupiter SD, Jenkins AP, et al. Mobile genes in the human microbiome are structured from global to individual scales. Nature. 2016;535(7612):435–439. doi:10.1038/nature18927.

62. Vos M, Didelot X. A comparison of homologous recombination rates in bacteria and archaea. ISME J. 2009;3(2):199–208. doi:10.1038/ismej.2008.93.

63. Guttman DS, Dykhuizen DE. Clonal divergence in *Escherichia coli* as a result of recombination, not mutation. Science. 1994;266:1380–1383.

64. Suerbaum S, Smith JM, Bapumia K, Morelli G, Smith NH, Kunstmann E, et al. Free recombination within Helicobacter pylori. Proc Natl Acad Sci U S A. 1998;95(21):12619–24.

65. Didelot X, Meric G, Falush D, Darling AE. Impact of homologous and non-homologous recombination in the genomic evolution of Escherichia coli. BMC Genomics. 2012;13:256. doi:10.1186/1471-2164-13-256.

66. Dixit PD, Pang TY, Studier FW, Maslov S. Recombinant transfer in the basic genome of Escherichia coli. Proc Natl Acad Sci U S A. 2015;112(29):9070–5. doi:10.1073/pnas.1510839112.

67. Dixit PD, Pang TY, Maslov S. Recombination-driven genome evolution and stability of bacterial species. Genetics. 2017;207:281–295.

68. Ochman H, Lawrence JG, Groisman EA. Lateral gene transfer and the nature of bacterial innovation. Nature. 2000;405:299–304.

69. Good BH, Desai MM. Deleterious passengers in adapting populations. Genetics. 2014;198:1183–1208.

70. Whitlock MC. Fixation probability and time in subdivided populations. Genetics. 2003;164:967–779.

71. Karasov T, Messer PW, Petrov DA. Evidence that adaptation in *Drosophila* is not limited by mutation at single sites. PLoS Genetics. 2010;6:e1000924.

72. Tenaillon O, Rodríguez-Verdugo A, Gaut RL, McDonald P, Bennett AF, Long AD, et al. The Molecular Diversity of Adaptive Convergence. Science. 2012;335:457–461.

73. Ghalayini M, Launay A, Bridier-Nahmias A, Clermont O, Denamur E, Lescat M, et al. Evolution of a dominant natural isolate of *Escherichia coli* in the human gut over a year suggests a neutral evolution with reduced effective population size. Applied and environmental microbiology. 2018; p. AEM–02377.

74. Zhao S, Lieberman TD, Poyet M, Groussin M, Gibbons SM, Xavier RJ, et al. Adaptive evolution within the gut microbiome of individual people. bioRxiv. 2017; p. 208009.

75. Press MO, Wiser AH, Kronenberg ZN, Langford KW, Shakya M, Lo CC, et al. Hi-C deconvolution of a human gut microbiome yields high-quality draft genomes and reveals plasmid-genome interactions. bioRxiv. 2017; p. 198713.

76. Moss E, Bishara A, Tkachenko E, Kang JB, Andermann TM, Wood C, et al. De novo assembly of microbial genomes from human gut metagenomes using barcoded short read sequences. bioRxiv. 2017; p. 125211.

77. Wattam AR, Davis JJ, Assaf R, Boisvert S, Brettin T, Bun C, et al. Improvements to PATRIC, the all-bacterial Bioinformatics Database and Analysis Resource Center. Nucleic Acids Res. 2017;45(D1):D535–D542. doi:10.1093/nar/gkw1017.

78. Wu D, Jospin G, Eisen JA. Systematic identification of gene families for use as "markers" for phylogenetic and phylogeny-driven ecological studies of bacteria and archaea and their major subgroups. PLoS One. 2013;8(10):e77033. doi:10.1371/journal.pone.0077033.

79. Chen Y, Ye W, Zhang Y, Xu Y. High speed BLASTN: an accelerated MegaBLAST search tool. Nucleic Acids Res. 2015;43(16):7762–8. doi:10.1093/nar/gkv784.

80. Langmead B, Salzberg S. Fast gapped-read alignment with Bowtie 2. Nature Methods. 2012;9:357–359.

81. Li H, Handsaker B, Wysoker A, Fennell T, et al. The Sequence Alignment/Map format and SAMtools. Bioinformatics. 2009;25:2078–2079.

82. Birky CW Jr, Walsh JB. Effects of linkage on rates of molecular evolution. Proc Natl Acad Sci USA. 1988;85:6414–6418.

83. Deatherage DE, Barrick JE. Identification of mutations in laboratory-evolved microbes from next-generation sequencing data using breseq. Methods Mol Biol. 2014;1151:165–188.

84. Jones E, Oliphant T, Peterson P, et al.. SciPy: Open source scientific tools for Python; 2001–. Available from: `http://www.scipy.org/`.

85. Bobay LM, Ochamn H. Biological species are universal across Life's Domains. Genome Biol Evol. 2017;9:491–501.

86. Falush D, Wirth T, Linz B, Pritchard JK, et al. Traces of human migrations in *Helicobacter pylori* populations. Science. 2003;299:1582–1585.

87. Peter BM. Admixture, Population Structure, and F-Statistics. Genetics. 2016;202(4):1485–501. doi:10.1534/genetics.115.183913.

88. Pritchard JK, Stephens M, Donnelly P. Inference of population structure using multilocus genotype data. Genetics. 2000;155(2):945–59.

89. Rödelsperger C, Neher RA, Weller AM, Eberhardt G, Witte H, Mayer WE, et al. Characterization of Genetic Diversity in the Nematode *Pristionchus Pacificus* from Population-Scale Resequencing Data. Genetics. 2014;196:1153–1165.

90. Rocha EP, Smith JM, Hurst LD, Holden MT, et al. Comparisons of dN/dS are time dependent for closely related bacterial genomes. J Theor Biol. 2006;239:226–235.

91. McVean GAT. A Genealogical Interpretation of Linkage Disequilibrium. Genetics. 2002;162:987–991.

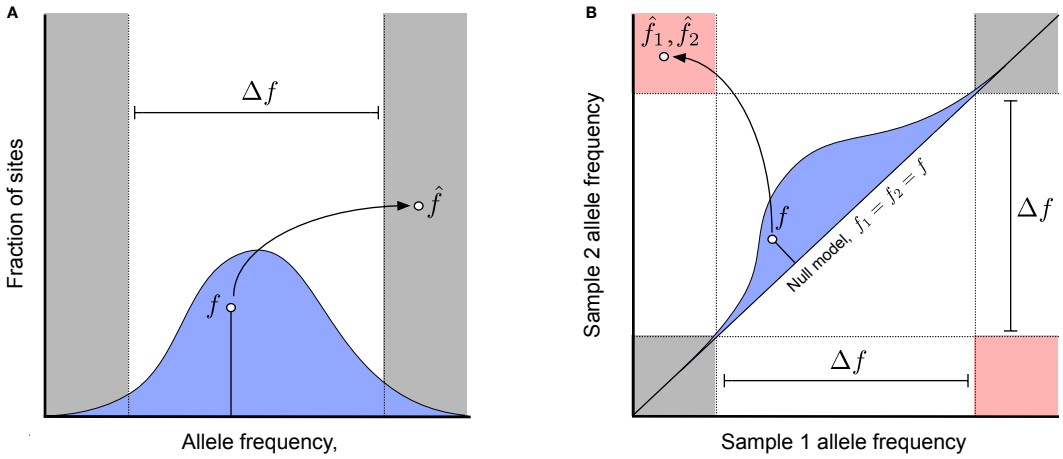

Fig S1. Schematic depiction of phasing and substitution errors. (a) An example of a haplotype phasing error, where an allele with true within-host frequency f [drawn from a hypothetical genome-wide prior distribution, $p_0(f)$, blue] is observed with a sample frequency $\hat{f}$ with the opposite polarization. (b) An example of a falsely detected nucleotide substitution between two samples, where an allele with true frequency $f_1 = f_2 = f$ [drawn from a hypothetical genome-wide null distribution, $p_0(f)$, blue] is observed with a sample frequency $\hat{f}_1 < 20\%$ in one sample and $\hat{f}_2 > 80\%$ in another. Allele frequency pairs that fall in the pink region are counted as nucleotide differences between the two samples, while pairs in the grey shaded region are counted as evidence for no nucleotide difference; all other values are treated as missing data.

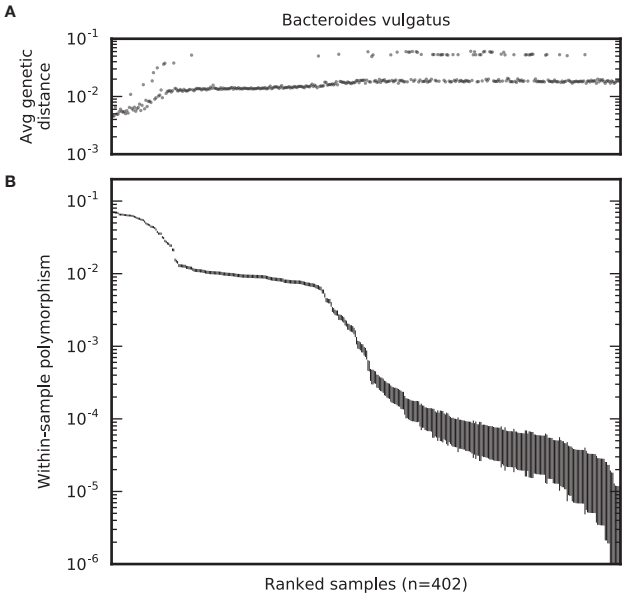

Fig S2. Average genetic distance between *B. vulgatus* metagenomes. (a) The fraction of fourfold degenerate synonymous sites in the core genome that have major allele frequencies $\geq 80\%$ and differ in a randomly selected sample (see Text S3.3 for a formal definition). (b) The corresponding rate of intermediate-frequency polymorphism for each sample, reproduced from Fig. 1B. In both panels, samples are plotted in the same order as in Fig. 1B.

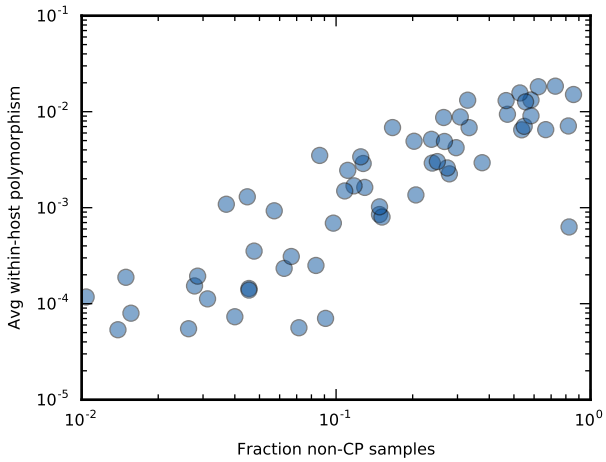

Fig S3. Correlation between within-host diversity and the fraction of non-QP samples per species. Circles denote the average rate of within-host polymorphism (as defined in Fig. 1E) for each species as a function of the fraction of non-QP samples in that species.

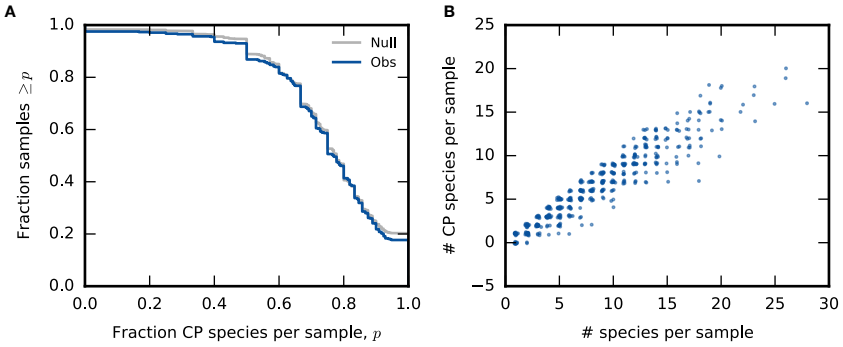

Fig S4. Distribution of the number of QP species per sample. Left: The distribution of the fraction of QP species per sample (blue line). The grey line denotes the corresponding null distribution obtained by randomly permuting the QP classifications across the samples. Right: The number of species classified as QP in each sample on the left as a function of the number of species in that sample. A small amount of noise is added to both axes to enhance visibility.

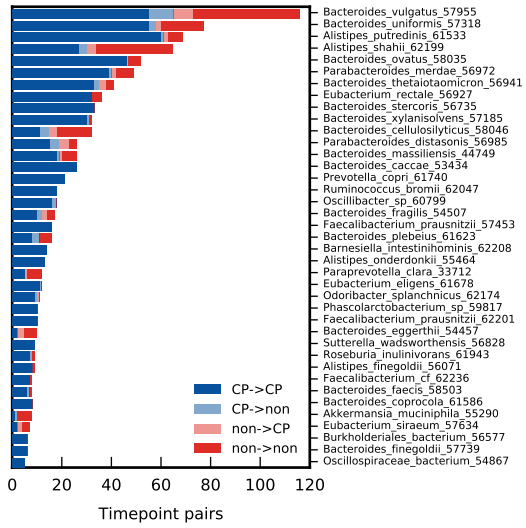

Fig S5. Distribution of quasi-phaseable (QP) samples in longitudinally sampled hosts. Species are arranged in decreasing order of prevalence. Only species with ≥ 5 longitudinally sampled individuals are included.

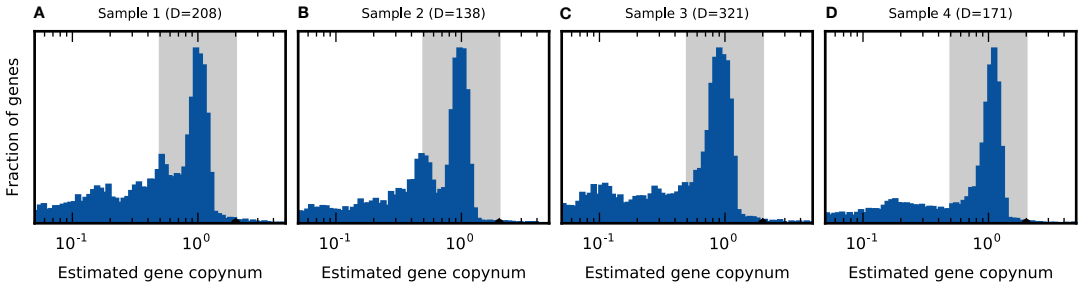

Fig S6. Distribution of estimated gene copy numbers for the four samples in Fig. 1. The grey region denotes the copy number range required in at least one sample to detect a difference in gene content between a pair of samples (see Text S3.5).

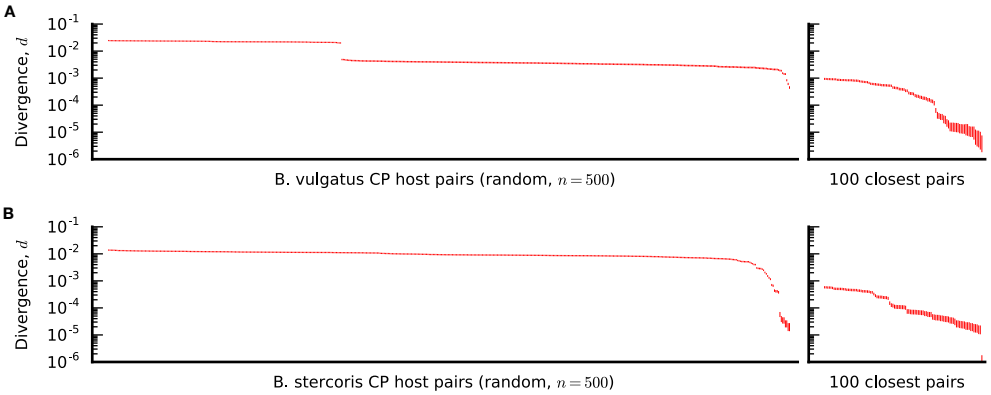

Fig S7. Distribution of nucleotide divergence between hosts for two *Bacteroides* species. Nucleotide divergence across the core genome of *B. vulgatus* for (a) 500 random host pairs, sorted in descending order, and (b) the 100 most closely related pairs, for comparison. For each pair, vertical lines denote 95% posterior confidence intervals based on the observed number of counts (SI Section S9 Text) (c,d). Analogous versions of panels (a) and (b) for *B. stercoris*.

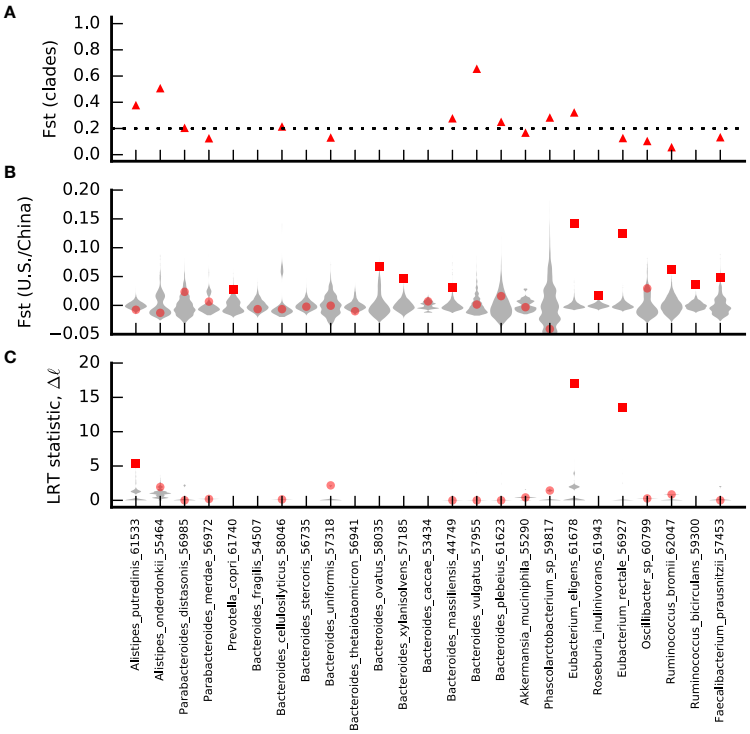

Fig S8. Geographic and clade structure among lineages in different QP hosts. Top panel: F_{st} between manually assigned top-level clades (i.e., groups of deeply diverged lineages in the lineage tree) for each species, as defined in Table S2. Species are only included if there are at least two clades with more than two individuals in each of them. The dashed line denotes the upper range of the middle panel below. Middle panel: F_{st} between HMP (US) and Chinese samples. Observed values are plotted as symbols, and the null distributions (obtained by randomly permuting country labels) are shown in grey. Significant F_{st} values ($p < 0.05$) are indicated with a square symbol. Bottom panel: likelihood ratio statistic assessing whether (manually assigned) clades are better predictors of country of origin. Species are included only if there are at least two clades with more than two individuals. Observed values are plotted as symbols (significant=square, non-significant=circle), while the null distributions (obtained by randomly permuting country labels) are shown in grey.

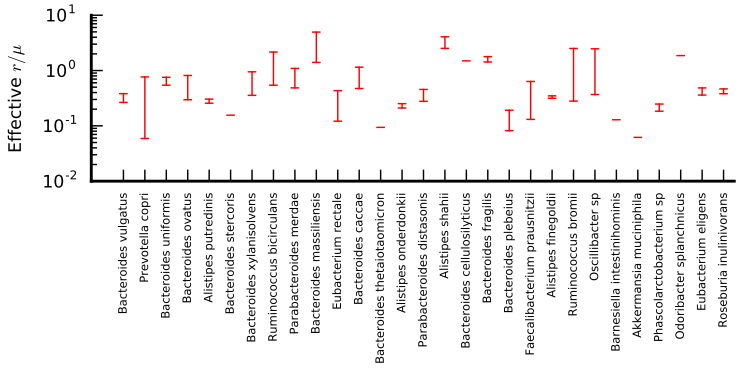

Fig S9. Recombination rate estimates based on the decay of linkage disequilibrium. For each species, the two dashes represent effective values of r/μ estimated from the neutral prediction for the decay of $\sigma_d^2(\ell)$, using the half-maximum and quarter-maximum decay lengths (see SI Section S6 Text). The two estimates are connected by a vertical line for visualization.

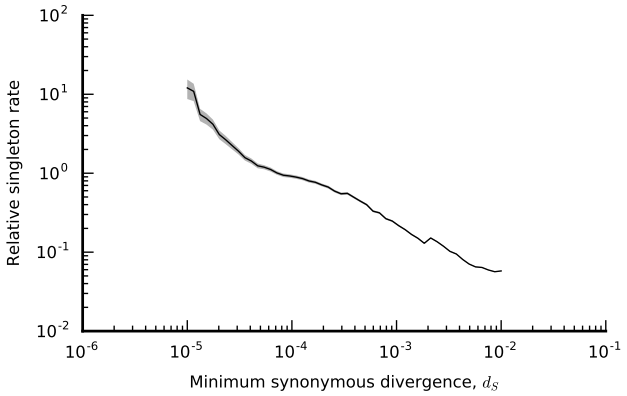

Fig S10. Enrichment of private SNVs in closely related lineages. An estimate of the relative singleton rate for all hosts that have core genome synonymous divergence $\leq d_S$ with the next most closely related host. For a given host i, the core genome synonymous divergence with the next closely related host is defined as $\min_j d_S^{ij}$, across all other hosts j. For a given value of d_S, the relative singleton rate is estimated by dividing the total number of synonymous singleton SNVs across all hosts with $\min_j d_S^{ij} \leq d_S$, by the corresponding number of opportunities, and then by the corresponding total of $\min_j d_S^{ij}$. The shaded region denotes a ±2 standard deviation confidence interval obtained by bootstrap resampling.

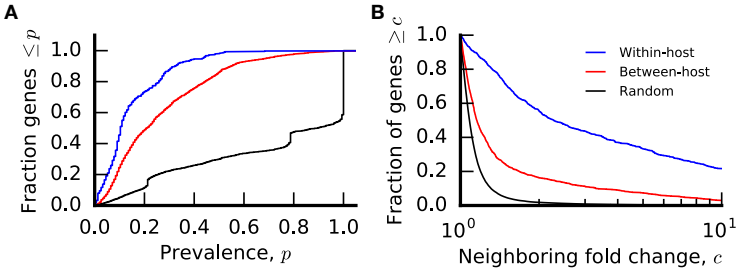

Fig S11. Properties of within-host gene changes in *B. vulgatus*. (a) Distribution of gene prevalence (fraction of hosts with copy number ≥ 0.3) for all genes (black), genes that differ between hosts (red), and genes that differ within hosts over time (blue). All calculations are restricted to the samples used in Fig. 5. (b) Distribution of fold change in copy number for genes immediately upstream and downstream of genes that differ within hosts over time (blue), a randomly selected gene (black), or genes that differ between hosts (red). Definitions of upstream and downstream are based on genome coordinates of the isolates used to construct the pangenome [33].

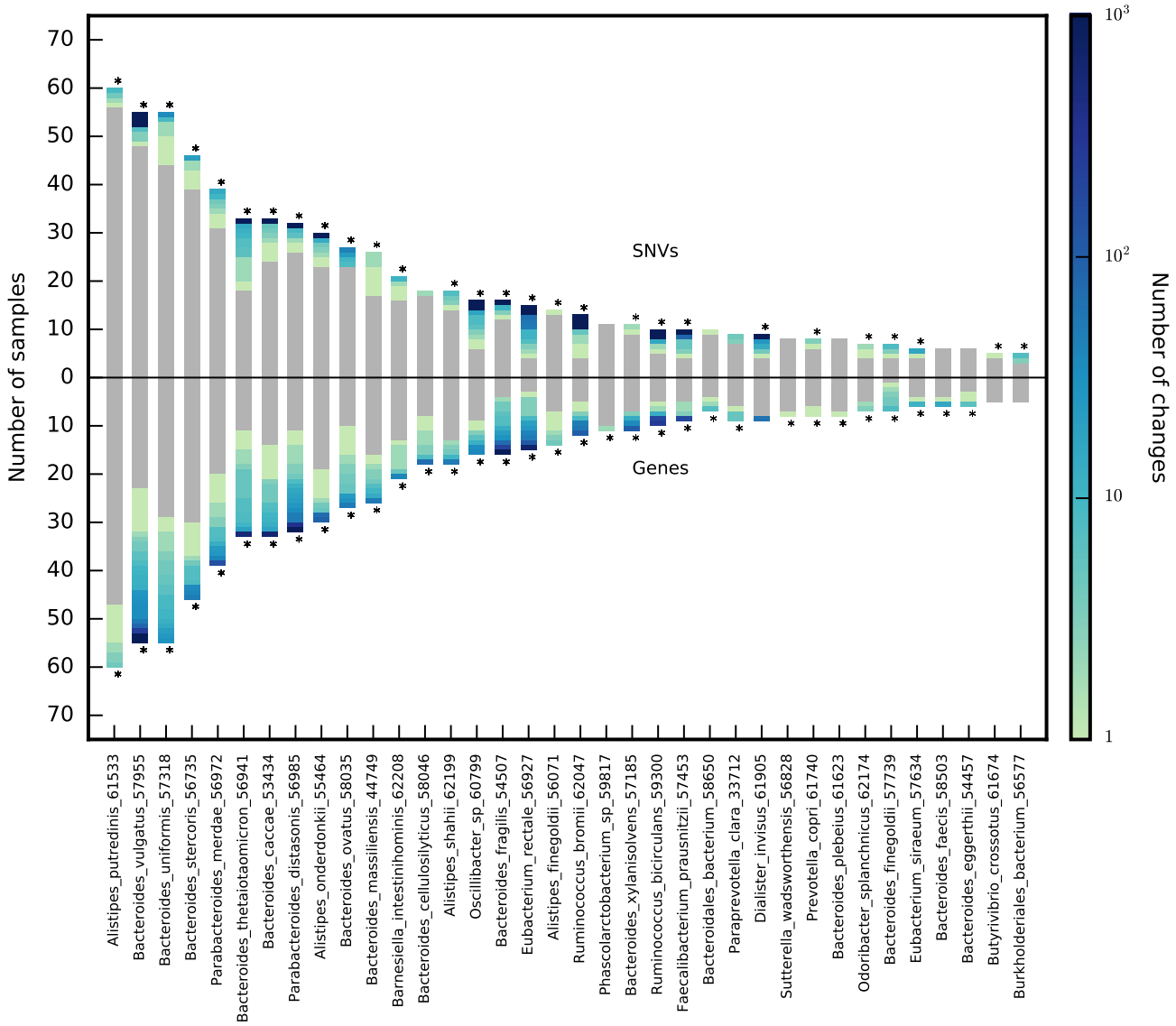

Fig S12. Comparable rates of within-host SNV and gene changes across prevalent species. Summary of within-host SNV changes (top) and gene changes (bottom) across all species with at least 5 pairs of longitudinal QP samples. Each row in each bar represents a different longitudinal pair, and rows are colored according to the total number SNV changes (top) and gene changes (bottom), with grey indicating no detected changes. A star indicates that the total number of non-replacement changes is ≥ 10 times the total estimated error rate across samples (see SI Sections S3.4 and S3.5), where replacements are defined as in Fig. 6.

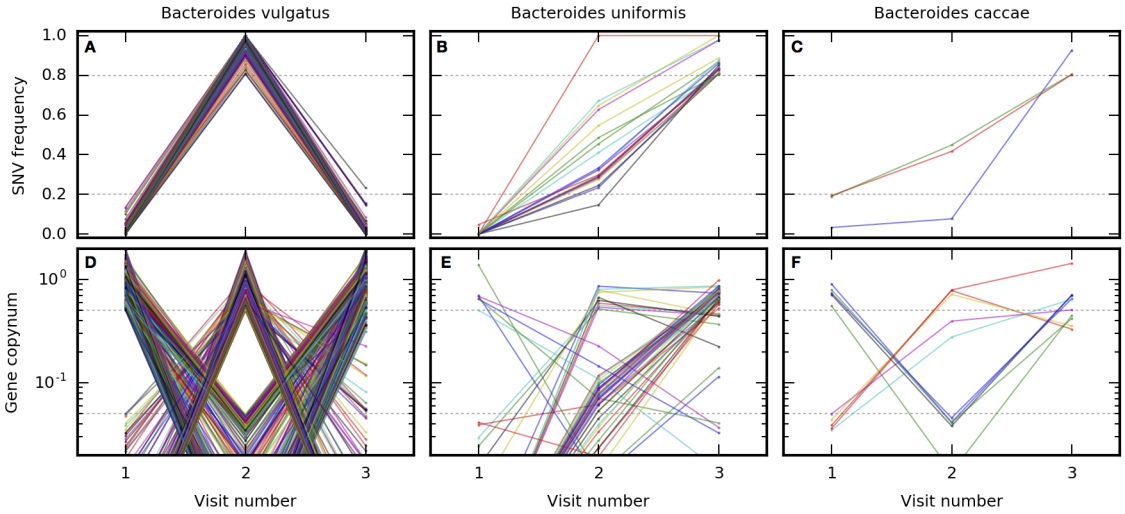

Fig S13. Examples of within-host changes in individuals sampled three times. SNV frequency trajectories (a-c) and gene copy number trajectories (d-f) as a function of visit number for three example host/species combinations (left, center, and right). Each line represents a different SNV or gene variant, and the lines are colored for visualization. In (a-c), allele frequencies are polarized according to the first visit number, and SNVs are only included if they have frequency $\leq 20\%$ at the first timepoint, and $\geq 80\%$ at one of the later timepoints (dashed lines). SNVs are excluded if they fail to meet the coverage requirements at any of the three timepoints. In (d-f), genes are only included if the initial copy number lies in either the present or absent regions (illustrated by dashed lines), and if at least one later timepoint is in the opposite state. Genes are excluded if they exceed the maximum copynumber ($c \leq 2$) at any of the three timepoints.

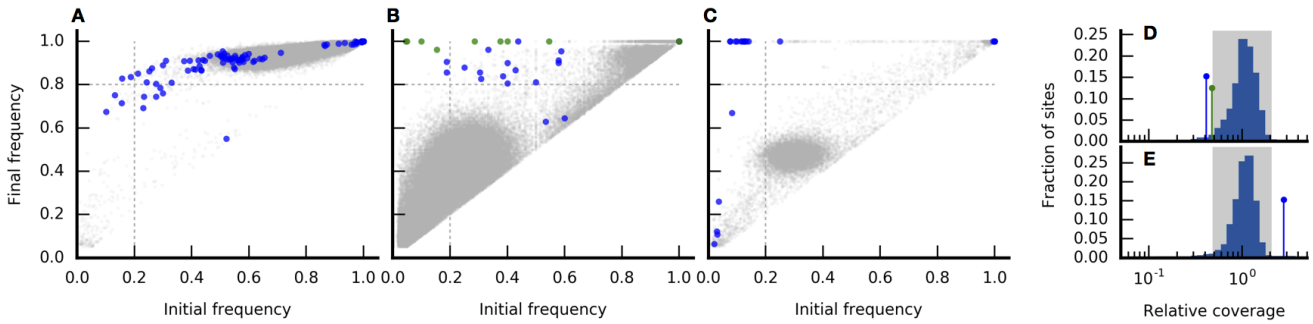

Fig S14. Examples of putatively clonal and local sweeps in *B. vulgatus*. (a-c) Final vs initial allele frequencies for all SNVs in the *B. vulgatus* genome in three pairs of longitudinal samples whose initial timepoint was classified as non-QP. Allele frequencies are polarized such that the change in allele frequency is positive. In each panel, SNVs are colored if they are in a gene with at least two detected SNV changes that are more than 100bp apart. Different genes in the same panel are assigned different colors for clarity. All other SNVs are colored grey. SNVs are only plotted if they had sufficient coverage at both timepoints, and if at least one timepoint had allele frequency ≥ 0.05. Panel (a) illustrates a putatively clonal sweep, while panels (b) and (c) suggest local sweeps. (d) The distribution of relative coverage at all core-genome sites at the initial timepoint in panel (b). The median coverage for the colored sites in (b) is indicated with the corresponding line and symbol. (e) An analgous version of (d) for the individual in panel (c). Note that in both (d) and (e), the sweeping genes are outliers in the coverage distribution.

Table S1. Metagenomic samples used in study. We analyzed 1576 samples from the Human Microbiome Project (HMP), and 185 samples from Ref. [43]. Listed are the subject ids, sample ids, run accessions, country of the study, continent of the study, visit number, and study (HMP or Qin *et al*, 2012).

Table S2. Top-level clade definitions. This table contains the manually-defined top-level clades described in Text S4.1. Rows list the various combinations of species and hosts plotted in Fig. 3, along with its corresponding numeric clade label.

Table S3. Gene change annotations. All genes that changed across the species analyzed in Fig. 6B were annotated with the PATRIC [77] database. Several genes were grouped into a single category based on keyword matches as described in SI Section S8 Text. Listed are the total number of gene changes, the expected number of changes assuming a null comprised of all changes between hosts, a null comprised of all genes present in hosts at all time points, and a null comprised of genes present in the pangenome. Expectations are also listed for gene gains and loss using the same three nulls. Lastly, the names of genes that are grouped together in a single keyword category are listed.

Table S4. SNV change annotations. An analogous version of Table S3 for genes that harbored a within-host SNV change. Listed are the total number of genes with at least one SNV change between consecutive timepoint pairs, and the expected number of hits under a null comprised of all changes between hosts and a null comprised of all genes present in hosts at all time points. Lastly, the names of genes that are grouped together in a single keyword category are listed.

S1 Text

Variant calling

S1.1 Overview

We analyzed whole-genome sequence data from a panel of 499 stool samples from 365 healthy human subjects (Table S1). Of these, 185 samples from China (all unique subjects) were previously sequenced by Ref. [43], and 314 samples from North America were from 180 subjects from the Human Microbiome Project [42] (87 individuals sampled once; 52 sampled 2 times roughly 6 months apart; 41 individuals sampled 3 times over the span of ~ 1 year). Previous work has shown that there is little genomic variability between technical and sample replicates in HMP data [33, 44], so we merged fastq files for technical and sample replicates from the same time point to increase coverage to resolve within-host allele frequencies.

We analyzed the gene and SNV content of these samples using the MIDAS software package [v1.2.2 [33]], with custom filters and postprocessing scripts. MIDAS first quantifies the relative abundances of species in different metagenomic samples by mapping sequencing reads to a database of universal single-copy "marker" gene sequences [33, 78] using HS-BLASTN [79]. Based on this step, species with average marker gene coverage ≥ 3 are defined as "present" in a given sample. These species are then concatenated to create a sample-specific reference genome and corresponding reference pangenome for the SNV and gene content estimation steps using the default MIDAS database (version 1.2, downloaded on November 21, 2016). To minimize potential mapping artifacts in detecting changes in longitudinally sampled individuals, we counted a species as present in all timepoints for a given individual if it was deemed present in any single timepoint, and this larger set of species was used to construct a consistent set of reference genomes and pangenomes across the different timepoints.

S1.2 Quantifying gene content

To quantify gene content in each sample, sequencing reads were aligned to the sample-specific pangenome using Bowtie2 [80] with default MIDAS settings: local alignment, MAPID ≥94.0%, READQ ≥20, and ALN_COV ≥0.75. We note that with these settings, reads with multiple best-hit alignments will be distributed among these targets according to their proportional representation on the pangenome reference sequence.

For each species, average coverage was reported for each gene after clustering at 95% sequence identity, as well as for a panel of universal, single-copy marker genes [33, 78]. Gene content was only evaluated in species with marker coverage ≥ 20 in a given sample. The ratio between gene and marker coverage was used to estimate the copy number of each gene in the sample. We used this information to define a "core genome" for each species, defined as the set of all genes with copy number ≥ 0.3 in $\geq 90\%$ of hosts in our panel. All other genes were defined to be "accessory" genes.

Given the limitations of our short-read approach, we cannot definitely prove that a read came from a particular species, particularly in the case of highly conserved or highly promiscuous genes. We therefore restricted our downstream analyses to genes with copynumbers in the range $0 \leq c \leq 0.05$ ("absent") and $0.5 \leq c \leq 2$ ("present"), in order to reduce potential cases where fluctuations in species abundance would lead to erroneous gene content changes. In principle, sequence data with longer-range linkage information [41] could be used to confirm that any gene content differences are linked with the appropriate core-genome backbone.

S1.3 Identifying SNVs

To identify putative SNVs, sequencing reads were aligned to sample-specific reference genomes using Bowtie2, with default MIDAS mapping thresholds: global alignment, MAPID ≥94.0%, READQ ≥20, ALN_COV ≥0.75, and MAPQ ≥20. After alignment, species were only retained if at least 40% of the reference genome had coverage ≥ 1. MIDAS reports reference and SNV allele counts using samtools mpileup [81]. We defined the within-sample allele frequency to be the fraction of reference alleles at a given site. (When present, multiple alternative alleles are therefore merged into a single allele.)

For each species, we then calculated the distribution of coverage at all sites in the core genome in each sample. We used this information to define a characteristic coverage value $\overline{D}$ for each sample, defined as the median of all core genome sites with nonzero coverage. To ensure adequate coverage for accurately estimating allele frequencies, samples with $\overline{D} < 20$ were excluded from further analyses. To further reduce mapping artifacts, sites in a given sample were masked (assigned zero coverage) if their coverage was $< 0.3\overline{D}$ or $\geq 3\overline{D}$. For similar reasons, we only considered SNVs in coding sequences of annotated genes, and we masked sites with nonzero coverage in fewer than 4 samples across our panel.

When comparing groups of samples, we defined a site to be a potential SNV candidate if it had within-host frequency $> 5\%$ in at least one sample. To avoid including sites due to rounding biases, we stipulated that the frequency must exceed 5% by at least $1/D$. All other sites were assumed to be monomorphic in that comparison. When analyzing a single sample (e.g. in Figs. 1A-D and Text S3.2), all sites were included regardless of allele frequency.

S2 Text

Within-host evolution in a single-colonization model

In this section, we further explain the assumptions made in computing the expected within-host polymorphism rate for a given species under a simple, single-colonization model. As described in the text, we will make conservatively high estimates for the per site mutation rate ($\mu \sim 10^{-9}$ per generation), generation times ($\lambda \sim 10$ generations per day), and time since colonization ($\Delta t \sim 100$ years). We define the within-host polymorphism rate P as the fraction of fourfold-degenerate synonymous site mutations with allele frequencies in the range $0.2 \leq f \leq 0.8$. In the single-colonization model, the mutations that contribute to P must have reached intermediate frequencies after starting as a *de novo* mutation at some time after colonization.

We assume that the synonymous mutations are effectively neutral over the timespans considered ($s\lambda\Delta t \ll 1$). Under this assumption, one of these mutations can only contribute to P if it hitchhiked along with a lineage that rose to a frequency in the range $0.2 \leq f \leq 0.8$. This can happen either due to neutral drift (i.e., the lineage randomly fluctuated to intermediate frequencies) or selection (i.e., the lineage reached intermediate frequencies because it contains a beneficial mutation). However, if synonymous mutations are neutral, their presence or absence in a lineage is independent of the processes that drive it to intermediate frequency [82]. The probability that a particular neutral mutation arose along the line of descent is simply the product of the per-site mutation rate μ and the total number of generations since the lineage diverged from the common ancestor between it and the rest of the population. By assumption, the latter is bounded by the total number of generations since colonization ($\lambda\Delta t$). This yields the conservative estimate for the within-host polymorphism rate,

$$P \leq \mu\lambda\Delta t \leq 10^{-3}, \tag{S2.1}$$

quoted in the main text.

S3 Text

Quasi-phasing metagenomic samples

In this section, we describe the methods used to estimate one of the dominant haplotypes for a given species in a subset of metagenomic samples (the so-called *quasi-phaseable* or QP samples), and to quantify genetic differences between these lineages. The method is similar in spirit to recent work by Ref. [35], but with a greater emphasis on estimating the associated false positive rates.

S3.1 Theoretical motivation

To gain intuition for how within-host lineage structure is reflected in the distribution of allele frequencies, it is useful to start by considering the simplest version of the phasing problem, in which the metagenomic reads for a given species in a particular sample are derived one of two clonal lineages mixed in a proportion $f_{\text{mix}} \geq 50\%$ (representing the proportion of cells from the more abundant lineage). Within-sample polymorphisms will arise from fixed differences between the two lineages and will segregate at frequency f_{mix} or $1 - f_{\text{mix}}$, depending on which lineage the mutation arose in and the choice of reference allele. Since this choice is arbitrary, we work with the major allele frequency in each sample. In this case, the distribution of major allele frequencies, $p(f)$, will then have the simple form

$$p(f) = (1 - d) \cdot \delta(1 - f) + d \cdot \delta(f - f_{\text{mix}}), \tag{S3.1}$$

where d is the average nucleotide divergence between the two lineages and $\delta(z)$ is the Dirac delta function. Note that this theoretical distribution is only obtained in the limit of infinite coverage; in practice, the observed distribution of major allele frequencies will be blurred due to sampling noise (see Text S3.2 below). Nevertheless, in the the limit of high coverage, Eq. (S3.1) suggests that we can infer f_{mix} and d by looking for a peak in the distribution of major allele frequencies (e.g., Fig. 1E). Again, in the idealized case, the two haplotype sequences are easy to recognize: major alleles are assigned to the dominant lineage, while the minor alleles belong to the subdominant type.

This basic idea also extends to mixtures of more than two lineages, but the potential genealogical relationships between them make the problem much more complicated. For example, in a mixture of three strains with frequencies f_1, f_2, and f_3, the distribution of major allele frequencies will now have three characteristic peaks (corresponding to $\min\{f_i, 1 - f_i\}$ for each $i = 1, 2, 3$). This time, however, alleles that segregate at the same frequency do not necessarily belong to the same lineage, since they could also be ancestral to two of the three strains. There are three possible genealogies relating the three strains, which can vary from site-to-site in the presence of recombination. Haplotype estimation then becomes a complicated inference problem, which only grows more difficult as additional lineages are added. Consideration of the combined allele frequency distribution may be helpful for deriving error models for algorithms that attempt to deconvolute strains from metagenomes.

Rather than trying to infer the exact mixture proportions and the haplotypes of each lineage, we developed a set of heuristic rules to identify the haplotype of just *one* of the dominant lineages while controlling the probability of misassigning variants to this haplotype. Suppose that there are within-sample polymorphisms at two sites, with major allele frequencies f_1 and f_2. We denote the four (unobserved) two-locus haplotype frequencies by f_{MM}, f_{Mm}, f_{mM}, and f_{mm}, where M and m denote the major and minor allele at each site. If $f_1 = f_2 = 0.5$, then there are no constraints on the possible haplotype frequencies, other than the marginal constraints $f_{MM} + f_{Mm} = f_1$ and $f_{MM} + f_{mM} = f_2$. However, in the opposite extreme where $f_1 = f_2 = 1$, then normalization constraints require that $f_{MM} = 1$ (i.e., the major alleles are on the same haplotype). In between these two extremes there is a more general rule that, whenever the allele

frequencies satisfy $f_i \geq f$, with $\log(f/1-f) = c \gtrsim 1$, the minimum possible frequency of the MM haplotype is

$$f_{MM} \geq 2f - 1 \sim 1 - 2e^{-c} \,. \tag{S3.2}$$

Equation S3.2 represents a worst case scenario in which the haplotypes are specifically assigned to prevent major alleles from segregating together. In practice, a more realistic lower bound for the f_{MM} is attained when the alleles are in linkage equibrium:

$$f_{MM} = f^2 \sim 1 - 2e^{-c} \,, \tag{S3.3}$$

which happens to have the same asymptotic behavior in this two-locus example. In either case, these bounds show that an appreciable fraction of cells in the host must possess both major alleles.

This argument can also be extended to larger collections of sites. In the pessimistic case of linkage equilibrium between all polymorphic sites, the number of major alleles per individual is binomially distributed with success probability f. In the limit of a large number of sites, this means that the vast majority of the cells will have the major allele at a fraction f of the possible sites. However, while the haplotype consisting of all major alleles is the most likely haplotype under linkage equilibrium, its expected frequency can grow quite small, to the point where the haplotype may not even be present in a finite sample. Fortunately, our analysis will primarily focus on one- and two-locus statistics where the stronger bounds in Eq. (S3.2) can be applied.

S3.2 False positive rate for SNP phasing

The arguments above suggest that, for many downstream purposes, we can effectively estimate a portion of one of the haplotypes in a metegenomic sample by taking the major alleles present above some threshold freuqency, $f^* \gg 50\%$, and treating sites with intermediate frequencies as missing data. This is a simple generalization of the consensus method (i.e. taking the haplotype formed by all major alleles) that has been used in previous metagenomic studies [4, 35], and it is similar to methods used to genotype clonal isolates from whole-genome resequencing data [83].

The major difficulty with this approach is that we do not observe the true frequency f directly, but rather a sample frequency $\hat{f}$ that is estimated from a finite number of sequencing reads. Polarization errors (i.e. errors in determining the major allele) can therefore accumulate when the allele supported by the most reads differs from true major allele in the sample. When sequencing clonal isolates, such false positives are primarily caused by sequencing errors. These occur at a low rate per read ($p_{\text{err}} \sim 1\%$ per bp), and become increasingly unlikely at moderate sequencing depths. However, in a metagenomic sample, polarization errors will also arise due to finite sampling noise, when an allele at some intermediate frequency (e.g. 25%) happens to be sampled in a majority of the sequencing reads. As we will show below, for moderate sequencing depths, this will often be the dominant source of error.

To model this process, let (A_ℓ, D_ℓ) denote the number of alternate alleles and total sequencing depth at a given site ℓ in the genome, and let $\hat{f}_\ell = A_\ell/D_\ell$ denote the corresponding sample frequency. We assume that the number of alternate reads follows a binomial distribution,

$$\Pr[A_\ell | D_\ell, f_\ell] = \binom{D_\ell}{A_\ell} f^{A_\ell}(1-f)^{D_\ell - A_\ell} \,, \tag{S3.4}$$

for some true frequency f_ℓ, so that the probability of observing $\hat{f}_\ell \geq f^*$ is simply

$$\Pr[\hat{f}_\ell \geq f^* | D_\ell, f_\ell] = \sum_{k \geq f^* D_\ell} \binom{D_\ell}{k} f^k (1-f)^{D_\ell - k} \,. \tag{S3.5}$$

A polarization error will occur when we observe $\hat{f}_\ell \geq f^*$ even though $f_\ell < 50\%$. Equation (S3.5) shows the probability of such an error will strongly depend on f_ℓ. For a sequencing depth of

$D = 10$ and a frequency threshold of $f^* = 80\%$, the error probability ranges from essentially negligible ($\sim 10^{-14}$) when f is on the order of the sequencing error rate ($\sim 1\%$), to ~ 1 per bacterial genome when $f \approx 10\%$, to an error rate of 5% when $f \approx 50\%$.

The average false positive rate across the genome will therefore depend on an average over the possible values of f and D:

$$\Pr[\text{error}] = \int \Pr[\hat{f} \geq f^* | D, f] p_0(D, f)\, dD\, df\,, \tag{S3.6}$$

where $p_0(D, f)$ is the prior distribution of D and f at a randomly chosen site (Fig. S1A). In the absence of any additional information, this joint distribution with the product of empirical distributions,

$$p_0(D, f) \approx \hat{p}(D)\hat{p}(f)\,, \tag{S3.7}$$

which we estimate for a given sample by binning the observed values of D and the allele frequencies across the L sites under consideration (blue distribution in Fig. S1A). The expected number of polarization errors in a given sample across all L sites is given by

$$N_{\text{err}} = \Pr[\text{error}] \times L\,. \tag{S3.8}$$

This calculation holds for any large collection of sites where the empirical distribution, $\hat{p}(f)$, provides a reasonable approximation to the prior distribution, $p_0(f)$. For example, in the following section, we consider the set of all synonymous sites in the core genome.

S3.3 Quasi-phaseable (QP) samples

The basic idea behind our approach is that we wish to restrict our attention to samples where N_{err} is small compared to the total number of sites under consideration. This number will vary depending on the particular analysis that we wish to carry out. But for population-genetic purposes, it will always be related to the number of sites that actually vary between samples. As a simple proxy for this number, we therefore consider a measure of the average genetic distance between the dominant haplotype in a given sample and the lineages in the remainder of our panel.

Specifically, we focus on fourfold-degenerate synonymous sites in the core genome. For each sample, let $N_<$ denote the number of such sites with major allele frequencies less than f^*, and conversely, let $N_>$ denote the number of sites with $\hat{f} \geq f^*$. For the sites in the latter group, let $\overline{f}_\ell$ denote the corresponding allele frequency across the entire panel. Then the quantity

$$N_d = \sum_{\ell=1}^{L} (1 - \overline{f}_\ell) \tag{S3.9}$$

approximates the expected number of differences at these sites for an "average" individual drawn from the panel. A normalized version (N_d/L) is illustrated for the *B. vulgatus* samples in Fig. S2. We declare the sample to be a **quasi-phaseable (QP)** sample if it passes the coverage thresholds in SI Section S1 Text and $N_</N_d < 0.1$.

To see why this is a reasonable definition, we return to our error formula in Eq. (S3.8) and plug in conservative estimates for $p_0(D, f)$. For example, we expect that the number of truly polymorphic sites in the sample will also be of order $\sim N_d$, with the remaining sites having frequencies near the sequencing error threshold, $f \sim 1\%$. We then divide the remaining polymorphic sites into the fraction $N_</N_d \lesssim 0.1$ with major allele frequencies below f^*, and the remaining fraction ($\sim 100\%$) with major allele frequencies above f^*. If we make the conservative approximation that all of the sites in the latter group have minor allele frequencies $f \approx 1 - f^*$, and all of the sites in the former group have $f \approx 50\%$, then we obtain an approximate prior distribution for f:

$$\hat{p}_0(f) \approx \frac{N_> - N_d}{N_> + N_<}\delta(f - 0.01) + \frac{N_d}{N_> + N_<}\delta(f - 1 + f^*) + \frac{N_<}{N_> + N_<}\delta(f - 0.5)\,. \tag{S3.10}$$

If we make a similarly conservative approximation for the coverage distribution,

$$\hat{p}(D) \approx \delta(D - 10), \tag{S3.11}$$

where δ is the Dirac function, then for a threshold of $f^* = 80\%$, the realized false positive rate is

$$\begin{aligned}\frac{N_{\rm err}}{N_d} &\approx \frac{N_> - N_d}{N_d}\Pr[\hat{f} \geq f^*|10, 0.01] + \Pr[\hat{f} \geq f^*|10, 1 - f^*] + \frac{N_<}{N_d}\Pr[\hat{f} \geq f^*|10, 0.5] \\ &\lesssim 0.01\,.\end{aligned} \tag{S3.12}$$

Thus, with these thresholds, we expect that only a small fraction of informative sites (as defined by the average distance between samples) will be susceptible to polarization errors.

S3.4 False positive rate for SNV differences

Although the QP sample classification is a good rule of thumb for determining when polarization errors are more or less likely to happen, there are scenarios where we wish to measure genetic distances between samples (e.g. longitudinal samples from the same individual) that are much more closely related than an average pair of individuals in our panel. In these cases, the realized false positive rate can be much higher than the estimate in Eq. (S3.12). To obtain more accurate estimates of the error in these cases, we extend our calculation above to the specific problem of detecting the number of nucleotide differences between two samples.

Generalizing from the phasing problem above, we would conclude that the haplotypes in two samples share the same allele at a given site if that allele is present above frequency f^* in both samples. To observe a difference between the two samples, the allele would have to be present above frequency f^* in one sample and below $1 - f^*$ in another. If the allele lies between $1 - f^*$ and f^* in one of the samples, the site is treated as censored data. Under this definition, a nucleotide difference requires a change in allele frequency of at least

$$\Delta f = f^* - (1 - f^*) = 2f^* - 1\,. \tag{S3.13}$$

If we rewrite everything in terms of Δf, a nucleotide difference requires the allele frequency to lie below $(1 - \Delta f)/2$ in one sample and above $(1 + \Delta f)/2$ in another (pink shaded regions in Fig. S1B). We will adopt the latter notation here, as it allows us to easily consider more stringent thresholds for which $\Delta f > 2f^* - 1$.

Under the null hypothesis, we assume that the true allele frequency f is the same in the two samples. If we let D_1 and D_2 denote the coverage of the site in the two samples, then a simple generalization of Eq. (S3.6) shows that the false positive rate for a randomly chosen site is given by

$$\begin{aligned}\Pr[\text{error}] = \int \Big\{&\Pr[\,\hat{f}_1 \geq (1 + \Delta f)/2\,|D_1, f]\left(1 - \Pr[\hat{f}_2 \geq (1 - \Delta f)/2\,|D_2, f]\right) \\ &+ \left(1 - \Pr[\hat{f}_1 \geq (1 - \Delta f)/2\,|D_1, f]\right)\Pr[\,\hat{f}_2 \geq (1 + \Delta f)/2\,|D_2, f]\Big\} \\ &\times p_0(D_1, D_2, f)\, dD_1 dD_2 df\,,\end{aligned} \tag{S3.14}$$

where $\Pr[\hat{f} \geq f]$ is defined in Eq. (S3.5) and $p_0(D_1, D_2, f)$ is the prior distribution for D_1, D_2, and f at a random site. As in Eq. (S3.7) above, we estimate this prior distribution as a product of empirical distributions,

$$p_0(D_1, D_2, f) \approx \hat{p}(D_1)\hat{p}(D_2)\hat{p}(f) \tag{S3.15}$$

which we estimate by binning the observed values of D_1, D_2, and $\hat{f}_i$ across the genomes of the two samples (the blue distribution in S1B). The expected number of false positive substitutions is

then given by

$$N_{\mathrm{err}} = \Pr[\mathrm{error}] \times L\,. \tag{S3.16}$$

where L is the total number of sites compared between the two samples. This will vary depending on the application (e.g. synonymous sites, sites in core genes, all coding sites, etc. are used at various times in the main text).

The error estimate in Eq. (S3.16) is an implicit function of the threshold Δf. Given the typical sequencing coverages and allele frequency distributions of the QP samples in our analyses, we usually obtain sufficiently low error estimates (i.e., $N_{\mathrm{err}} \ll 1$) if we take $\Delta f = 1 - 2f^* = 0.6$, so that an allele transitions from less than 20% to greater than 80% frequency between the two samples, or vice versa. However, for the few outlier sample pairs where $N_{\mathrm{err}} > 0.5$, we attempted to increase Δf until $N_{\mathrm{err}}(\Delta f) \leq 0.5$. If this was not possible, we discarded that pair of samples from further analysis.

S3.5 False positive rate for gene content differences

The false positive rate for gene content differences can be estimated with a similar procedure. In this case, the canonical generative model is one in which a gene g with average copy number per cell $c_{g,i}$ in sample i recruits $N_{g,i}$ reads, which we assume follows a Poisson distribution:

$$N_{g,i} \sim \mathrm{Poisson}\left(c_{g,i} L_g F_i\right)\,, \tag{S3.17}$$

where L_g is the length of gene g and F_i is a sample- and species-specific constant that reflects the total number of reads aligned to that species (e.g., by the MIDAS pipeline). The coverage of gene g is then defined as

$$D_{g,i} = \frac{L_{r,i}}{L_g} \cdot N_{g,i} \equiv \frac{N_{g,i}}{\ell_{g,i}}\,, \tag{S3.18}$$

where $L_{r,i}$ is the average length of reads that align to that gene (typically $\lesssim$ 100bp), which can vary in a sample-specific manner. The quantity $\ell_{g,i} \equiv L_g / L_{r,i}$ then serves as a conversion factor between the raw number of reads and the coverage. Finally, we assume (as in the MIDAS pipeline) that there is a known panel of marker genes ($g = m$) with fixed copy number per cell of $c_m \approx 1$ and a large target size, such that $N_{m,i} \approx \mathbb{E}[N_{m,i}] = L_m F_i$. This allows us to eliminate F_i and rewrite Eq. (S3.17) in terms of the marker coverage $D_{m,i}$ and the coverage-to-read conversion factor $\ell_{g,i}$:

$$N_{g,i} \sim \mathrm{Poisson}\left(c_{g,i} \ell_{g,i} D_{m,i}\right)\,, \tag{S3.19}$$

The variables $N_{g,i}$, $D_{g,i}$, and $D_{m,i}$ are all reported by MIDAS, which allowed us to estimate $c_{g,i}$ and $\ell_{g,i}$ for each gene in each sample:

$$c_{g,i} = \frac{D_{g,i}}{D_{m,i}}\,, \quad \ell_{g,i} = \frac{L_g}{L_{r,i}} \approx \frac{N_{g,i}}{D_{g,i}}\,. \tag{S3.20}$$

Based on the above error rate calculations, the gene copy number change events we are interested in are those in which a gene transitions from a "typical" copy number value ($0.5 \leq c \leq 2$, see Fig. S6) in one sample to a value close to zero ($c < 0.05$) in another. This does not cover all possible copy number change events, but focuses on the subset that are likely to be (i) statistically significant and (ii) less susceptible to other bioinformatic errors (e.g. read stealing or donating from other species).

Given this definition, the probability of an apparent copy number change happening by chance will again depend on the "true" copy number of the gene, c, as well as its effective coverage, ℓD.

Similar to Eq. (S3.14), the expected false positive rate for a randomly chosen gene is given by

$$\begin{aligned}\Pr[\text{error}] = \int \Big\{ & F_P(0.05\ell D_{m,1}; c\ell D_{m,1}) \left[F_P(2\ell D_{m,2}; c\ell D_{m,2}) - F_P(0.5\ell D_{m,2}; c\ell D_{m,2})\right] \\ & + \left[F_P(2\ell D_{m,1}; c\ell D_{m,1}) - F_P(0.5\ell D_{m,1}; c\ell D_{m,1})\right] F_P(0.05\ell D_{m,2}; c\ell D_{m,2})\Big\} \\ & \times p_0(\ell, c)\, d\ell\, dc\,,\end{aligned} \tag{S3.21}$$

where $F_P(k;\lambda)$ is the Poisson CDF and $p_0(\ell, c)$ is the null distribution of ℓ and c. Once again, we estimate this joint distribution with the product of empirical distributions,

$$p_0(\ell, c) \approx \hat{p}(\ell)\hat{p}(c)\,, \tag{S3.22}$$

which are estimated by binning the observed values of $\ell_{g,i}$ and $c_{g,i}$ across the two samples. To reduce mapping artifacts, we only bin ℓ-values from genes with copy number in the range $0.5 \leq c \leq 2$, which accounts for the bulk of the copy number distribution in a given sample (S6). The expected number of false positive gene changes is therefore given by

$$N_{\text{err}} = \Pr[\text{error}] \times n_{\text{pangenome}}\,, \tag{S3.23}$$

where $n_{\text{pangenome}}$ is the total number of genes tested (typically of order $\sim 10^4$). For the typical coverages in our dataset, this number is usually very small ($\ll 10^{-2}$). In the few cases where the coverage is sufficiently low that $N_{\text{perr}} > 0.5$, we discarded the sample pair from consideration.

S4 Text

Population structure across hosts

In this section, we describe the population structure of a given species across hosts and the methods used to analyzed the data based on between-host comparisons.

S4.1 Clustering and identification of top-level clades

For each species, we constructed core-genome dendrograms by hierarchically clustering the matrix of pairwise divergence rates averaged across the core genome, using the UPGMA method from SciPy [84]. Examples for *B. vulgatus* and *B. stercoris* are illustrated in Fig. 2. Based on these dendrograms, lineages were assigned to one or more "top-level" clades using a manual procedure, loosely designed to maximize the difference between inter- and intra-clade divergence at the most deeply diverged branches (Table S2). We adopted this manual procedure to capture clade structure that is inconsistent with a single cut through the dendrogram at a given level of divergence.

In Fig. S8A, we plot the fixation index, F_{st} for these manually defined clades:

$$F_{st} = 1 - \frac{\sum_{\text{clade},c} \sum_{i,j \in c} d_{ij}}{\sum_{\text{clade},c} \sum_{i,j \in c} 1} \frac{\sum_{i,j} 1}{\sum_{i,j} d_{ij}}, \tag{S4.1}$$

where c indexes the clades and d_{ij} is the average nucleotide divergence across core genes in hosts i and j. Several of the prevalent species have top-level clades with high F_{st} (with *B. vulgatus* serving as one of the more extreme cases). But this is not a universal pattern across gut bacteria: some species, even other *Bacteroides* like *Bacteroides stercoris*, have lineage phylogenies more consistent with a single clade (Fig. 2C).

S4.2 Phylogenetic inconsistency

We quantify potential discrepancies between the core genome dendrograms in Figs. 2A,C and the genealogies of local genomic regions by defining a measure of *phylogenetic consistency* based on the fraction of homoplasic SNVs (i.e., SNVs that appear to conflict with the core genome dendrogram, see below). Our measure is conceptually similar to recent work by Ref. [85].

For a given core-genome divergence threshold d, we obtain a set of non-overlapping clade groupings $C(d)$ by cutting the UPGMA dendrogram in Fig. 2 at distance d. Then, for each clade $c \in C(d)$, we calculate the total number of core-genome sites that are polymorphic within the clade (n_c^p), as well as the subset that are also polymorphic among the remaining individuals in the population (n_c^i). We refer to the latter as *phylogenetically inconsistent* SNVs, since they are homoplasic at the given level of the genealogy. The net measure of phylogenetic inconsistency in Figs. 2B,D is then defined as the fraction of phylogenetically inconsistent SNVs across all the clades at the given level of divergence:

$$p(d) = \frac{\sum_{c \in C(d)} n_c^i}{\sum_{c \in C(d)} n_c^p}. \tag{S4.2}$$

Note that according to this definition, the same site may be included in the denominator multiple times if it is polymorphic in multiple clades. The same site can also be included for multiple divergence thresholds d.

In general, the overall magnitude of $p(d)$ can be influenced by factors other than the underlying rate of homoplasy. In particular, the probability of observing a phylogenetically inconsistent SNV will strongly depend on its allele frequency, as well as the size distribution of the various clades. To interpret the observed values of $p(d)$, we compared them to a null model of free recombination

that controls for these statistical biases. For each polymorphic site identified above, we generated a bootstrapped version by permuting the observed alleles across the set of hosts, while requiring that the site remains polymorphic within the clade of interest. This produces a bootstrapped dataset with the same values of n_c^p, but with a number of inconsistent sites $n_c^{i,0}$ that reflects the free recombination model. The overall level of phylogenetic inconsistency in this model is then defined as

$$p_0(d) = \frac{\sum_{c \in C(d)} n_c^{i,0}}{\sum_{c \in C(d)} n_c^p}, \tag{S4.3}$$

and is included as a grey line in Figs. 2B,D.

S4.3 Geographic structure

As described in the text, the between-host dendrogram for the *Bacteroides vulgatus* (Fig. 2A) does not appear to correlate strongly with the geographic location of the hosts. This lies in contrast to some other bacterial species, e.g. *Heliobacter pylori* [86] which possess more striking patterns of geographic differentiation. To investigate whether this pattern holds in other prevalent gut species, we calculated the fixation index, F_{st}, between U.S. and Chinese samples using an analgous version of Eq. (S4.1) (with clades replaced by countries). Figure S8 shows the observed F_{st} values for the set of species in Fig. 3. Apart from *E. rectale* and *E. eligens*, these F_{st} values are relatively low ($F_{st} < 0.1$), consistent with previous comparisons between the U.S. and European samples [31]. To assess the significance of these F_{st} values, we compared them to a null model in which the country labels were randomly permuted between the samples. This revealed 5 additional species with lower F_{st} values (i.e., < 0.1) with P-values less than 0.05 (Fig. S8B).

The F_{st} statistic can suffer from low power when the two groups are not perfectly partitioned into clades, even if the clades still preferentially harbor hosts from specific countries. To test for such residual geographic structure, we focused on the top-level clades in Table S2. We then asked whether the country of origin was preferentially associated with certain clades. To quantify this tendency, we calculated a likelihood ratio score,

$$\Delta\ell = \sum_{\text{clade},c} n_c^{U.S.} \log\left(\frac{p_c}{\overline{p}}\right) + n_c^{China} \log\left(\frac{1-p_c}{1-\overline{p}}\right), \tag{S4.4}$$

where $n_c^{U.S.}$ and n_c^{China} are the observed number of U.S. and Chinese samples in each clade, p_c is the expected fraction of U.S. samples in each clade, and $\overline{p}$ is the expected fraction of U.S. samples in the entire panel. Only clades with ≥ 2 samples are included in the sum. To focus on the most biologically significant differences, we set

$$p_c = \begin{cases} \frac{n_c^{U.S.}}{n_c^{U.S.}+n_c^{China}} & \text{if } \left|\log\left(\frac{p_c}{1-p_c}\frac{1-\overline{p}}{\overline{p}}\right)\right| \geq 1, \\ \overline{p} & \text{else.} \end{cases} \tag{S4.5}$$

To assess the significance of the observed likelihood ratio scores, we compared them to a null model in which the country labels were randomly permuted between the samples (Fig. S8C). Once again, *E. rectale* and *E. eligens* are highly significant, but the remaining species have much weaker signals.

Our analysis is not meant to imply that there is no geographic structure in the species we have considered, but rather that it does not appear to be the main driver of the genome-wide patterns that we observe. There may be additional strongly differentiated clades that were not sampled in our limited panel, or more pronounced geographic structure for genetic differences below our detection threshold. In addition, there may also be strong signals of population structure among individual loci, even if they are averaged out in the genome-wide distances that we consider. More sophisticated methods [e.g. F statistics [87] or programs like STRUCTURE [88]] could be used to investigate this further. These are interesting avenues for future work.

S5 Text

Population genetic null model of purifying selection for pairwise divergence

In this section, we present a minimal model of purifying selection that can account for the varying d_N/d_S levels in Fig. 3D as a function of d_S. The basic idea is that purifying selection is less efficient at purging deleterious mutations that are very young (in particular, younger than the inverse of the associated fitness cost). To the extent that synonymous divergence can be associated with a characteristic timescale, this line of reasoning implies that anomalously low values of d_S would be associated with less efficient purifying selection (i.e., higher values of d_N/d_S), while typical values of d_S would be associated with more efficient purifying selection (i.e., lower values of d_N/d_S). Similar ideas have been employed in previous studies [89, 90].

To make this idea more concrete, suppose that the age of a given mutation is bounded by a time T, so that it occured at some point in the last T generations. This will result in a genetic difference between two randomly sampled lineages with probability

$$d = \mathbb{E}\left[\int_0^T 2N(-t)\mu f(0;-t)(1-f(0;-t))\,dt\right], \tag{S5.1}$$

where $N(t)$ is the population size, $f(t;t_0)$ is the frequency of an allele that was created at time t_0 and sampled at time t, and the expectation is taken over all possible realizations of $f(t,t_0)$. If T is much smaller than the typical coalescence timescale of the population, then the mutation cannot rise to a very high frequency by the time of sampling, and we can neglect the f^2 term above to obtain

$$d \approx 2\mu \int_0^T \mathbb{E}[N(-t)f(0,-t)]\,dt\,. \tag{S5.2}$$

By definition, the new mutation will arise at frequency $1/N(-t)$. If the mutation has a deleterious fitness cost s, then its average size is simply

$$\mathbb{E}[N(-t)f(0,-t)] = e^{-st} \tag{S5.3}$$

and we have

$$d \approx 2\mu T \cdot \frac{1-e^{-sT}}{sT} \tag{S5.4}$$

If synonymous mutations are assumed to be neutral, we simply have $\mathbb{E}[d_S] = 2\mu T$ as expected. If we assume that the nonsynonymous sites have a distribution of deleterious fitness costs $\rho(s)$, then the nonsynonymous divergence rate satisfies

$$\frac{d_N}{d_S} \approx \int \frac{1-e^{-sT}}{sT}\rho(s)\,ds\,. \tag{S5.5}$$

In the simplest case, $\rho(s)$ will contain a mixture of truly neutral mutations and a fraction f_d with deleterious fitness cost s, for which

$$\frac{d_N}{d_S} \approx (1-f_d) + f_d \cdot \frac{1-e^{-sT}}{sT}\,. \tag{S5.6}$$

In order to connect this model with the observed data, we must find a way to estimate T. We assume that for anomalously low core-genome-wide divergence rates, the divergence time $d_S/2\mu$ provides a reasonable estimate of the maximum mutation age T at most polymorphic loci

(otherwise, we would expect a more typical value of d_S). Based on this assumption, we obtain an empirical relation between d_N/d_S and d_S:

$$\frac{d_N}{d_S} \approx (1-f) + f_d \cdot \frac{1 - e^{-\frac{s d_S}{2\mu}}}{\frac{s d_S}{2\mu}}, \tag{S5.7}$$

which is valid for d_S much smaller than the population median. For small d_S, this ratio will start to deviate from unity when $d_S \gtrsim 4\mu/sf$. At large d_S, the ratio approaches $1 - f_d$, and will start to deviate from this value when $d_S \lesssim 2\mu f_d/s(1-f_d)$. These landmarks allow us to obtain approximate estimates of f_d and s by rough inspection of the data in Fig. 3D.

We note that qualitatively similar behavior is expected in recent models of bacterial evolution proposed by Ref. [66], in which the core genome of closely related strains consists of an asexual "backbone" or "clonal frame" (where synonymous mutations occur at rate μ) interrupted by highly diverged segments of length ℓ_r acquired through recombination. The introgressed segments would enter with low values of d_N/d_S associated with the average d_S value. If the common ancestor of the asexual backbone is younger than the typical deleterious fitness cost, we would again expect a transition from essentially neutral behavior ($d_N/d_S \approx 1$) to the typical between-host value ($d_N/d_S \approx 0.1$) as a function of d_S, where the transition is now informative of the horizontal transfer rate. A formal analysis of this model remains an interesting avenue for future work.

S6 Text

Population genetic null model for the decay of linkage disequilibrium

In principle, the rate of decay of linkage disequilibrium in Fig. 4 contains information about the average recombination rate between pairs of loci [16]. For example, in a neutral panmictic population of size N, Ref. [53] have shown that

$$\sigma_d^2 = \frac{10 + 2NR}{22 + 26NR + 4(NR)^2}, \tag{S6.1}$$

where R is the recombination rate between two loci. Similar functional forms are expected for related measures of linkage disequilibrium (e.g. r^2 [91]). To obtain a relation between the recombination rate R and the genomic distance ℓ between two loci, we assume that recombination occurs through the exchange of DNA fragments of with average length ℓ_r, which are exponentially distributed around this mean value and occur uniformly across the genome. Two loci undergo a recombination event when there is a genetic exchange that involves only one of the two loci. This happens with probability

$$R(\ell) = r\ell_r \left(1 - e^{-\ell/\ell_r}\right), \tag{S6.2}$$

where r is a rate constant. Thus, for distances much shorter than ℓ_r, this recombination model resembles a linear chromosome with a crossover rate r per site. For larger distances, Eq. (S6.2) shows that the effective recombination rate saturates at $r\ell_r$. Substituting $R(\ell)$ into Eq. (S6.1), the decay of linkage disequilibrium will have the characteristic shape

$$\sigma_d^2 \sim \begin{cases} \frac{5}{11} & \text{if } \ell \ll \frac{1}{Nr}, \\ \frac{1}{2Nr\ell} & \text{if } \frac{1}{Nr} \ll \ell \ll \ell_r, \\ \frac{1}{2Nr\ell_r} & \text{if } \ell \gg \ell_r. \end{cases} \tag{S6.3}$$

To estimate $\sigma_d^2(\ell)$ for a given species, we focused on lineages from the largest top-level clade defined in Table S2. Since Fig. 3D suggests that evolutionary forces may be different for closely related strains, we chose only a single lineage from each subclade defined by cutting the core genome tree at divergence $d = 10^{-3}$. For pairs of SNVs in the same gene, we assigned a coordinate distance ℓ based on their relative position on the reference genome. For a given value of ℓ, we then estimated $\sigma_d^2(\ell)$ via

$$\hat{\sigma}_d^2(\ell) = \frac{\sum \widehat{(f_{AB} - f_A f_B)^2}}{\sum \widehat{f_A(1 - f_A) f_B(1 - f_B)}} \tag{S6.4}$$

where the sum runs over all pairs of synonymous sites with distances within the range $(\ell - \Delta\ell, \ell + \Delta\ell)$, as described in Fig. 4. Here, $f_A = f_{Ab} + f_{AB}$, and $f_B = f_{aB} + f_{AB}$, where f_{AB}, f_{Ab}, and f_{aB} denote the frequencies of the gametic combinations in the across-host population. The hat symbols denote unbiased esimators for the respective quantities underneath, based on the observed gamete counts n_{AB}, n_{Ab}, n_{aB}, and n_{ab} in our sample of hosts. We assume that the counts are sampled from the frequencies through the multinomial distribution,

$$\Pr[\vec{n}|\vec{f}] = \frac{n!}{n_{AB}! n_{Ab}! n_{aB}! n_{ab}!} f_{AB}^{n_{AB}} f_{Ab}^{n_{Ab}} f_{aB}^{n_{aB}} f_{ab}^{n_{ab}}, \tag{S6.5}$$

where $n = n_{AB} + n_{Ab} + n_{aB} + n_{ab}$ is the total sample size. The estimate for the hat symbols above are constructed via linear combinations of polynomials in the n's chosen to have the same

expected value as the quantity underneath the hat. These expressions are somewhat unwieldy, but are provided in the associated computer code.

After applying this method, we obtain estimates of within-gene $\sigma^2(\ell)$ as a function of ℓ, and a core-genome-wide value estimated from SNVs in different genes (Fig. 4), which can be compared with the theoretical prediction in Eq. (S6.3). Because the core-genome-wide value of σ_d^2 is usually much lower than its intragenic counterpart, we assume that ℓ_r is much larger than the ~ 3000bp intragenic window we consider, so we formally set $\ell_r = \infty$. However, it is also clear from Fig. 4 that $\sigma_d^2(\ell)$ does not always approach the neutral expectation as $\ell \to 0$. As is common practice, we therefore consider an expanded class of models of the form

$$\sigma_d^2(\ell) = C \cdot \frac{10 + 2Nr\ell}{22 + 26Nr\ell + 4(Nr\ell)^2} \tag{S6.6}$$

for some arbitrary normalization constant C, which must be jointly estimated from the data. (The introduction of C is equivalent to focusing on the percentage change in σ_d^2, rather than its absolute value.)

This model has two free parameters (Nr and C), which can be estimated from the observed values of σ_d^2 at any two values of ℓ. We fix one of these at a reference location $\ell_1 = 9$bp, which was chosen to balance the desire to have $\ell_1 \ll 1/Nr$, but also to be as large as possible to minimize contamination from compound mutation events. For the second value of $\sigma_d^2(\ell)$, we focus on distances of the form

$$\ell_p = \min\left\{\ell \,:\, \frac{\sigma^2(\ell)}{\sigma^2(\ell_1)} \leq p\right\} \tag{S6.7}$$

for some fraction p (e.g., $p = 1/2$, $p = 1/4$, etc.). In other words, ℓ_p is the distance at which the observed value of $\sigma^2(\ell)$ first falls to a percentage p of its value at ℓ_1. According to the model in Eq. S6.6, these distances should satisfy

$$p \equiv \frac{\sigma_d^2(\ell_p)}{\sigma_d^2(\ell_1)} = \frac{10 + 2Nr\ell_p}{22 + 26Nr\ell_p + 4(Nr\ell_p)^2} \cdot \frac{22 + 26Nr\ell_1 + 4(Nr\ell_1)^2}{10 + 2Nr\ell_1} \tag{S6.8}$$

which depends only on Nr, in addition to the observed values of p, ℓ_1, and ℓ_p. Solving this function numerically, we obtain estimates for Nr for different values of p.

In the neutral model that leads to Eq. S6.1, the population size N can be estimated from the average pairwise divergence, $d_S = 2N\mu$. Thus, we normalize the estimated values of Nr by $d_S/2$ to obtain an estimate of the ratio r/μ for different values of p. As long as the model is a good description of the data, these estimates should be approximately independent of the choice of p. The observed deviations in r/μ as a function of p (Fig. S9) point to fundamental deviations from the model in Eq. (S6.6) that cannot be accounted for by simply varying the parameters. This suggests that the decay of $\sigma_d^2(\ell)$ may hold power for investigating departures from the simple neutral model above (e.g. to include hitchhiking, population structure, variation in recombination rate within genes, etc.).

S7 Text

Clonal and local sweeps within hosts

In this section, we describe a preliminary search for clonal and local sweeps in the longitudinal cohort from the Human Microbiome Project [42]. The results in the main text suggest that recombination is important for initially acquiring adaptive segments. The resulting selective sweep can then proceed in one of two ways. If recombination is rare, then the initial recombinant could sweep in a clonal fashion, purging any variation along the rest of the genome. If recombination is sufficiently common, then additional recombination events (either from the original donor strain, or within the focal population) could allow the adaptive variant to spread to many genetic backgrounds and sweep only in a local genomic region .

In principle, we can distinguish between these scenarios by checking whether diversity is maintained at more distant genomic loci during the sweep. However, the quasi-phaseable samples we have focused on so far are poorly suited for this purpose, since they were originally selected to have a low density of SNVs that start at intermediate frequencies within hosts. Instead, we turned to the subset of non-quasi-phaseable individuals in our panel that harbored a large number of intermediate frequency polymorphisms at the initial timepoint (Fig. S5). These samples no longer conform to the null model used to derive the false positive rate in Text S3.4, making it more difficult to distinguish true SNV changes from sampling noise. To guard against false positives, we therefore focused only on individuals with at least one gene with ≥ 2 independent SNV changes. We also required the independent SNV changes to be separated by more than 100bp, to ensure that they are supported by different sequencing reads.

In the case of a clonal sweep, we would expect the allele frequencies on the rest of the genome to shift with the SNVs on the focal gene. In a local sweep, the SNVs on the focal gene should sweep independently of most other intermediate-frequency SNVs. Across our panel, we can find examples of both behaviors. For example, in Fig. S14A, a small number of alleles shifted from low frequencies ($< 20\%$) to $\sim 90\%$, which potentially dragged a large number of marker SNVs to the same final frequency, a classic signature of a clonal sweep. In contrast, in Fig. S14B and C, SNVs in three genes swept and appear to have dragged the remaining SNVs in those gene to fixation in a manner similar to Fig. S14A. Yet the vast majority of genome-wide SNVs remained at intermediate frequencies, which is suggestive of a local sweep.

However, it is important to note that there is a purely clonal process that can produce this pattern. For example, if the sample begins as a mixture of two widely diverged strains (as it does in Fig. S14B and C), then large portions of the accessory genome will be present in only one of the two strains. If there is a clonal sweep in one of these genes, which does not disturb the coexistence between the two strains, then the sweeping allele will rise to 100% frequency in the reads that align to that gene. Meanwhile, the diversity at genes that are shared between the two strains will remain relatively stable, giving the appearance of a local sweep. Consistent with this hypothesis, the relative coverage of the two genes in Fig. S14B is on the lower end of the core-genome-wide distribution (Fig. S14D). This is not the case for the gene in Fig. S14C, although the coverage is still an outlier compared to the genome-wide distribution. Additional analysis of within-host haplotype patterns will therefore be required to determine whether these are true examples of local sweeps.

S8 Text

Functional parallelism in gene content variation within hosts

To investigate whether similar functional categories are enriched in gene content changes within hosts, we analyzed the annotations of these genes based on the annotations provided by the PATRIC database [77]. Specifically, for the set of genes in Fig. 6B, we grouped the corresponding PATRIC annotation strings based on several manually-defined keywords (Table S3). For example, all genes with the keyword 'Conjugative transposon protein' were grouped into a single category labeled 'transposon'. If the annotation string did not match any manually-defined category, a new category was created using the annotation string itself. The number of observed within-host changes in each category is listed in Table S3.

Since different categories will vary in the number of genes that are assigned to them, we compared the observed number of changes within category to the expected number of changes under three null models. We computed the expected number of gene changes by sampling the same number of gene changes as observed, and averaged the resulting values over 100 bootstrap iterations. The three null distributions we considered included: (1) Between-host gene differences, which allowed us to test whether of gene changes within a host are different from genes changes between hosts. Genes that changed recurrently between different pairs of hosts were counted multiple times in the null. (2) Genes present within hosts, which allowed us to test whether gene changes within hosts are different from any random gene present at either time point. Genes present at more than one time point were counted multiple times, while genes present at only 1 time point were counted once. (3) Pangenome, which allowed us to test whether the within-host gene changes are enriched for any gene categories compared to the total distribution of gene categories in the pangenome.

For recombination-related proteins, the categories of genes drawn from the between-host gene differences null distribution was similar to the observed data, reflecting that gene changes between hosts are likely similar to gene changes within hosts. The the categories of genes drawn from the pangenome also resembled the observed data, which is consistent with the pangenome being enriched for more accessory genes than are present on average within a host.

S9 Text

Posterior confidence intervals for per-site rate estimates

To obtain the approximate confidence intervals for the rates in Figs. 1E and S7, we used a standard Bayesian procedure based on a poisson approximation. We outline this here for completeness.

If we let L denote the total number of sites examined and let n denote the number of "successes" (intermediate frequency polymorphisms in the case of Fig. 1E and between host differences in Fig. S7), then we assume that n is drawn from a Poisson

$$n \sim \mathrm{Poisson}(rL), \tag{S9.9}$$

where r is the per site rate plotted in Figs. 1E and S7. Since r is a positive quantity that varies over many orders of magnitude, we use a uniform prior over $\log r$. After applying Bayes' rule, this yields a standard conjugate Gamma posterior distribution for r:

$$p(r|n, L) = \frac{L^n}{(n-1)!} r^{n-1} e^{-rL}. \tag{S9.10}$$

whose posterior mean is just

$$\int r p(r|n, L)\, dr = \frac{n}{L}, \tag{S9.11}$$

as expected. For all $n > 0$, we define a $1 - \alpha$ confidence interval to be the $\alpha/2$ and $1 - \alpha/2$ percentiles of this posterior distribution. In the case where $n = 0$, the posterior distribution is improper:

$$p(r|0, L) \propto r^{-1} e^{-rL}. \tag{S9.12}$$

In this case, we define the lower limit of the confidence interval to be 0, and the upper limit to be the point where $e^{-rL} \sim \alpha/2$.